Chapter 14

Image-based rendering

14.1 View interpolation . . . 683
  14.1.1 View-dependent texture maps . . . 685
  14.1.2 *Application*: Photo Tourism . . . 686
14.2 Layered depth images . . . 688
  14.2.1 Impostors, sprites, and layers . . . 688
  14.2.2 *Application*: 3D photography . . . 690
14.3 Light fields and Lumigraphs . . . 693
  14.3.1 Unstructured Lumigraph . . . 696
  14.3.2 Surface light fields . . . 696
  14.3.3 *Application*: Concentric mosaics . . . 698
  14.3.4 *Application*: Synthetic re-focusing . . . 698
14.4 Environment mattes . . . 699
  14.4.1 Higher-dimensional light fields . . . 700
  14.4.2 The modeling to rendering continuum . . . 701
14.5 Video-based rendering . . . 701
  14.5.1 Video-based animation . . . 702
  14.5.2 Video textures . . . 703
  14.5.3 *Application*: Animating pictures . . . 705
  14.5.4 3D and free-viewpoint Video . . . 706
  14.5.5 *Application*: Video-based walkthroughs . . . 708
14.6 Neural rendering . . . 711
14.7 Additional reading . . . 718
14.8 Exercises . . . 719

R. Szeliski, *Computer Vision*, Texts in Computer Science,
https://doi.org/10.1007/978-3-030-34372-9_14

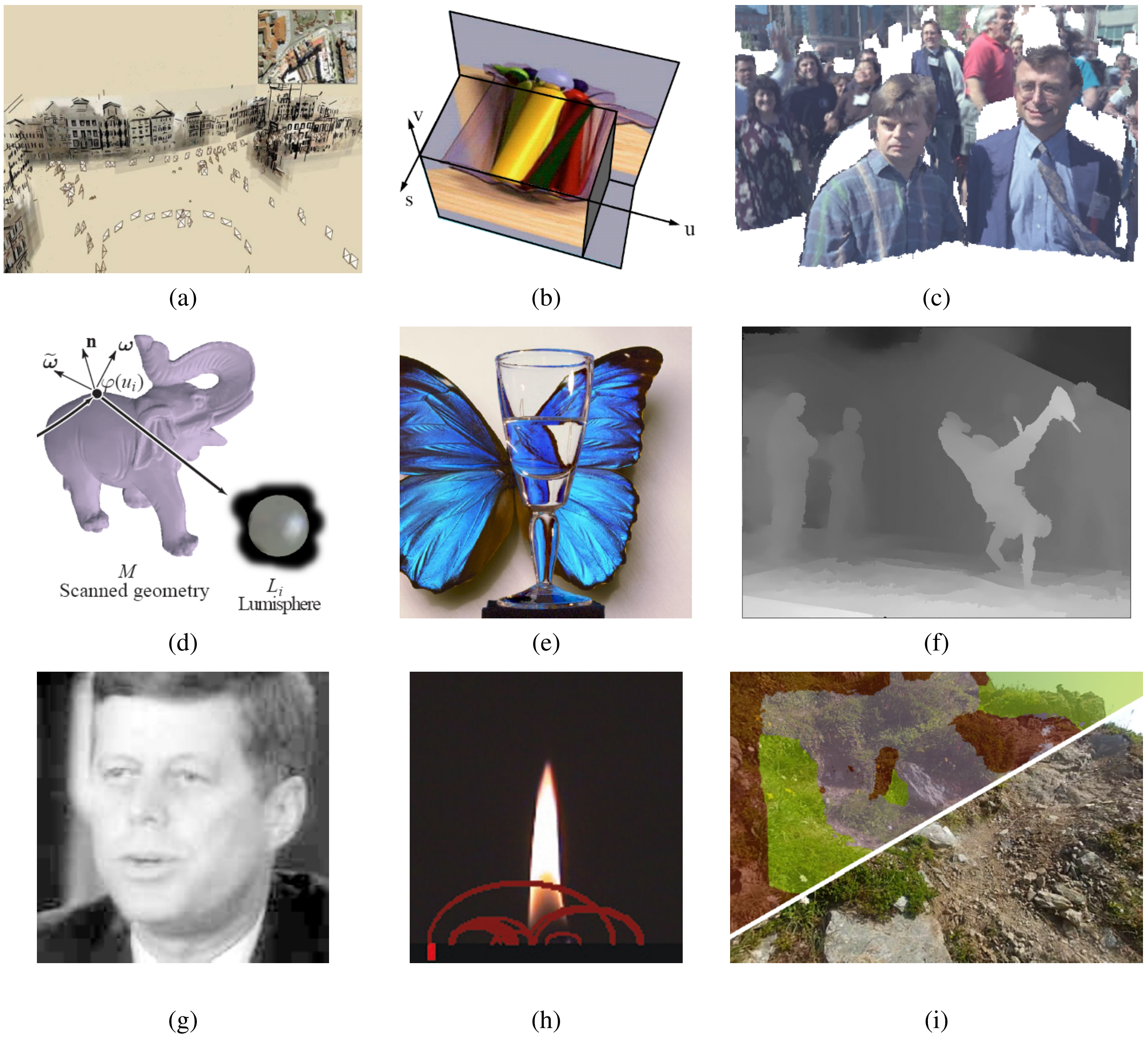

Figure 14.1 Image-based and video-based rendering: (a) a 3D view of a Photo Tourism reconstruction (Snavely, Seitz, and Szeliski 2006) © 2006 ACM; (b) a slice through a 4D light field (Gortler, Grzeszczuk *et al.* 1996) © 1996 ACM; (c) sprites with depth (Shade, Gortler *et al.* 1998) © 1998 ACM; (d) surface light field (Wood, Azuma *et al.* 2000) © 2000 ACM; (e) environment matte in front of a novel background (Zongker, Werner *et al.* 1999) © 1999 ACM; (f) video view interpolation (Zitnick, Kang *et al.* 2004) © 2004 ACM; (g) Video Rewrite used to re-animate old video (Bregler, Covell, and Slaney 1997) © 1997 ACM; (h) video texture of a candle flame (Schödl, Szeliski *et al.* 2000) © 2000 ACM; (i) hyperlapse video, stitching multiple frames with 3D proxies (Kopf, Cohen, and Szeliski 2014) © 2014 ACM.

Over the last few decades, image-based rendering has emerged as one of the most exciting applications of computer vision (Kang, Li *et al.* 2006; Shum, Chan, and Kang 2007; Gallo, Troccoli *et al.* 2020). In image-based rendering, 3D reconstruction techniques from computer vision are combined with computer graphics rendering techniques that use multiple views of a scene to create interactive photo-realistic experiences such as the Photo Tourism system shown in Figure 14.1a. Commercial versions of such systems include immersive street-level navigation in online mapping systems such as Google Maps and the creation of 3D Photosynths from large collections of casually acquired photographs.

In this chapter, we explore a variety of image-based rendering techniques, such as those illustrated in Figure 14.1. We begin with *view interpolation* (Section 14.1), which creates a seamless transition between a pair of reference images using one or more precomputed depth maps. Closely related to this idea are *view-dependent texture maps* (Section 14.1.1), which blend multiple texture maps on a 3D model's surface. The representations used for both the color imagery and the 3D geometry in view interpolation include a number of clever variants such as *layered depth images* (Section 14.2) and *sprites with depth* (Section 14.2.1).

We continue our exploration of image-based rendering with the *light field* and *Lumigraph* four-dimensional representations of a scene's appearance (Section 14.3), which can be used to render the scene from any arbitrary viewpoint. Variants on these representations include the *unstructured Lumigraph* (Section 14.3.1), *surface light fields* (Section 14.3.2), *concentric mosaics* (Section 14.3.3), and *environment mattes* (Section 14.4).

We then explore the topic of *video-based rendering*, which uses one or more videos To create novel video-based experiences (Section 14.5). The topics we cover include video-based facial animation (Section 14.5.1), as well as *video textures* (Section 14.5.2), in which short video clips can be seamlessly looped to create dynamic real-time video-based renderings of a scene.

We continue with a discussion of *3D videos* created from multiple video streams (Section 14.5.4), as well as *video-based walkthroughs* of environments (Section 14.5.5), which have found widespread application in immersive outdoor mapping and driving direction systems. We finish this chapter with a review of recent work in *neural rendering* (Section 14.6), where generative neural networks are used to create more realistic reconstructions of both static scenes and objects as well as people.

14.1 View interpolation

While the term *image-based rendering* first appeared in the papers by Chen (1995) and McMillan and Bishop (1995), the work on *view interpolation* by Chen and Williams (1993) is considered as the seminal paper in the field. In view interpolation, pairs of rendered images are combined with their precomputed depth maps to generate interpolated views that mimic what a virtual camera would see in between the two reference views. Since its original introduction, the whole field of *novel view synthesis* from captured images has continued to be a very active area. A good historical overview and recent results can be found in the CVPR tutorial on this topic (Gallo, Troccoli *et al.* 2020).

View interpolation combines two ideas that were previously used in computer vision and computer graphics. The first is the idea of pairing a recovered depth map with the reference image used in its computation and then using the resulting texture-mapped 3D model to generate novel views (Figure 12.1). The second is the idea of *morphing* (Section 3.6.3) (Figure 3.51), where correspondences between pairs of images are used to warp each reference image to an in-between location while simultaneously cross-dissolving between the two warped images.

Figure 14.2 illustrates this process in more detail. First, both source images are warped to the novel view, using both the knowledge of the reference and virtual 3D camera pose along with each

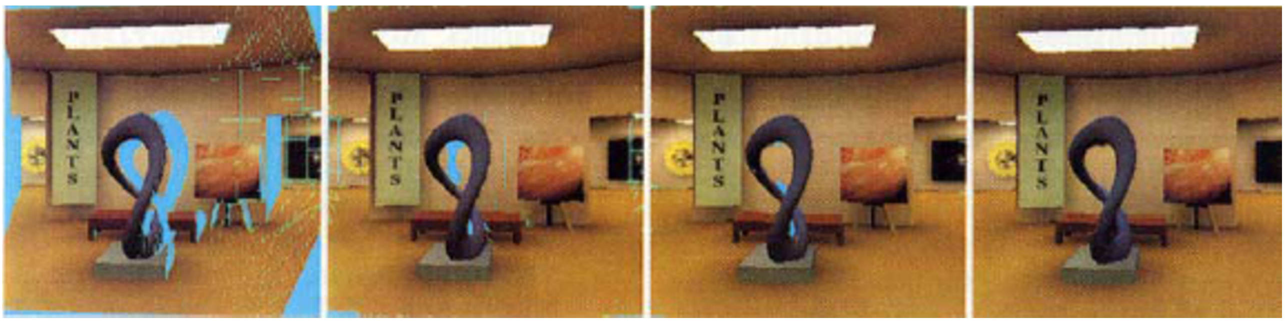

Figure 14.2 View interpolation (Chen and Williams 1993) © 1993 ACM: (a) holes from one source image (shown in blue); (b) holes after combining two widely spaced images; (c) holes after combining two closely spaced images; (d) after interpolation (hole filling).

image's depth map (2.68–2.70). In the paper by Chen and Williams (1993), a *forward warping* algorithm (Algorithm 3.1 and Figure 3.45) is used. The depth maps are represented as quadtrees for both space and rendering time efficiency (Samet 1989).

During the forward warping process, multiple pixels (which occlude one another) may land on the same destination pixel. To resolve this conflict, either a *z-buffer* depth value can be associated with each destination pixel or the images can be warped in back-to-front order, which can be computed based on the knowledge of epipolar geometry (Chen and Williams 1993; Laveau and Faugeras 1994; McMillan and Bishop 1995).

Once the two reference images have been warped to the novel view (Figure 14.2a–b), they can be merged to create a coherent composite (Figure 14.2c). Whenever one of the images has a *hole* (illustrated as a cyan pixel), the other image is used as the final value. When both images have pixels to contribute, these can be blended as in usual morphing, i.e., according to the relative distances between the virtual and source cameras. Note that if the two images have very different exposures, which can happen when performing view interpolation on real images, the hole-filled regions and the blended regions will have different exposures, leading to subtle artifacts.

The final step in view interpolation (Figure 14.2d) is to fill any remaining holes or cracks due to the forward warping process or lack of source data (scene visibility). This can be done by copying pixels from the *further* pixels adjacent to the hole. (Otherwise, foreground objects are subject to a "fattening effect".)

The above process works well for rigid scenes, although its visual quality (lack of aliasing) can be improved using a two-pass, forward–backward algorithm (Section 14.2.1) (Shade, Gortler *et al.* 1998) or full 3D rendering (Zitnick, Kang *et al.* 2004). In the case where the two reference images are views of a non-rigid scene, e.g., a person smiling in one image and frowning in the other, *view morphing*, which combines ideas from view interpolation with regular morphing, can be used (Seitz and Dyer 1996). A depth map fitted to a face can also be used to synthesize a view from a longer distance, removing the enlarged nose and other facial features common to "selfie" photography (Fried, Shechtman *et al.* 2016).

While the original view interpolation paper describes how to generate novel views based on similar precomputed (linear perspective) images, the *plenoptic modeling* paper of McMillan and Bishop (1995) argues that cylindrical images should be used to store the precomputed rendering or real-world images. Chen (1995) also proposes using environment maps (cylindrical, cubic, or spherical) as source images for view interpolation.

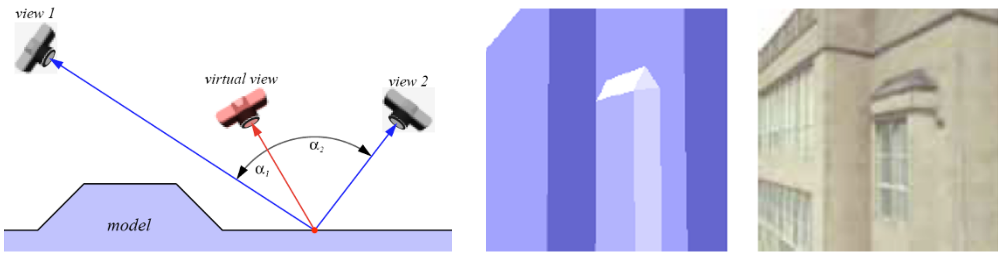

(a) (b) (c)

Figure 14.3 View-dependent texture mapping (Debevec, Taylor, and Malik 1996) © 1996 ACM. (a) The weighting given to each input view depends on the relative angles between the novel (virtual) view and the original views; (b) simplified 3D model geometry; (c) with view-dependent texture mapping, the geometry appears to have more detail (recessed windows).

14.1.1 View-dependent texture maps

View-dependent texture maps (Debevec, Taylor, and Malik 1996) are closely related to view interpolation. Instead of associating a separate depth map with each input image, a single 3D model is created for the scene, but different images are used as texture map sources depending on the virtual camera's current position (Figure 14.3a).[1]

In more detail, given a new virtual camera position, the similarity of this camera's view of each polygon (or pixel) is compared to that of potential source images. The images are then blended using a weighting that is inversely proportional to the angles α_i between the virtual view and the source views (Figure 14.3a).[2] Even though the geometric model can be fairly coarse (Figure 14.3b), blending different views gives a strong sense of more detailed geometry because of the visual motion between corresponding pixels. While the original paper performs the weighted blend computation separately at each pixel or coarsened polygon face, follow-on work by Debevec, Yu, and Borshukov (1998) presents a more efficient implementation based on precomputing contributions for various portions of viewing space and then using projective texture mapping (OpenGL-ARB 1997).

The idea of view-dependent texture mapping has been used in a large number of subsequent image-based rendering systems, including facial modeling and animation (Pighin, Hecker *et al.* 1998) and 3D scanning and visualization (Pulli, Abi-Rached *et al.* 1998). Closely related to view-dependent texture mapping is the idea of blending between light rays in 4D space, which forms the basis of the Lumigraph and unstructured Lumigraph systems (Section 14.3) (Gortler, Grzeszczuk *et al.* 1996; Buehler, Bosse *et al.* 2001).

To provide even more realism in their Façade system, Debevec, Taylor, and Malik (1996) also include a *model-based stereo* component, which computes an offset (parallax) map for each coarse planar facet of their model. They call the resulting analysis and rendering system a *hybrid geometry- and image-based* approach, as it uses traditional 3D geometric modeling to create the global 3D model, but then uses local depth offsets, along with view interpolation, to add visual realism. Instead of warping per-pixel depth maps or coarser triangulated geometry (as in unstructured Lumigraphs, Section 14.3.1), it is also possible to use super-pixels as the basic primitives being warped (Chaurasia, Duchene *et al.* 2013). Fixed rules for view-dependent blending can also be replaced with deep neural networks, as in the *deep blending* system by Hedman, Philip *et al.* (2018).

[1]The term *image-based modeling*, which is now commonly used to describe the creation of texture-mapped 3D models from multiple images, appears to have first been used by Debevec, Taylor, and Malik (1996), who also used the term *photogrammetric modeling* to describe the same process.

[2]More sophisticated blending weights are discussed in Section 14.3.1 on unstructured Lumigraph rendering.

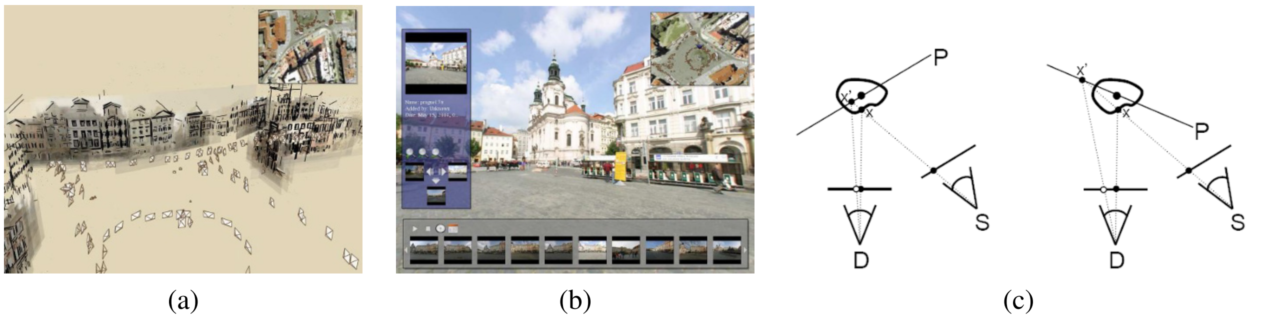

Figure 14.4 Photo Tourism (Snavely, Seitz, and Szeliski 2006) © 2006 ACM: (a) a 3D overview of the scene, with translucent washes and lines painted onto the planar impostors; (b) once the user has selected a region of interest, a set of related thumbnails is displayed along the bottom; (c) planar proxy selection for optimal stabilization (Snavely, Garg *et al.* 2008) © 2008 ACM.

14.1.2 *Application*: Photo Tourism

While view interpolation was originally developed to accelerate the rendering of 3D scenes on low-powered processors and systems without graphics acceleration, it turns out that it can be applied directly to large collections of casually acquired photographs. The *Photo Tourism* system developed by Snavely, Seitz, and Szeliski (2006) uses structure from motion to compute the 3D locations and poses of all the cameras taking the images, along with a sparse 3D point-cloud model of the scene (Section 11.4.6, Figure 11.17).

To perform an image-based exploration of the resulting *sea of images* (Aliaga, Funkhouser *et al.* 2003), Photo Tourism first associates a 3D proxy with each image. While a triangulated mesh obtained from the point cloud can sometimes form a suitable proxy, e.g., for outdoor terrain models, a simple dominant plane fit to the 3D points visible in each image often performs better, because it does not contain any erroneous segments or connections that pop out as artifacts. As automated 3D modeling techniques continue to improve, however, the pendulum may swing back to more detailed 3D geometry (Goesele, Snavely *et al.* 2007; Sinha, Steedly, and Szeliski 2009). One example is the hybrid rendering system developed by Goesele, Ackermann *et al.* (2010), who use dense per-image depth maps for the well-reconstructed portions of each image and 3D colored point clouds for the less confident regions.

The resulting image-based navigation system lets users move from photo to photo, either by selecting cameras from a top-down view of the scene (Figure 14.4a) or by selecting regions of interest in an image, navigating to nearby views, or selecting related thumbnails (Figure 14.4b). To create a background for the 3D scene, e.g., when being viewed from above, non-photorealistic techniques (Section 10.5.2), such as translucent color washes or highlighted 3D line segments, can be used (Figure 14.4a). The system can also be used to annotate regions of images and to automatically propagate such annotations to other photographs.

The 3D planar proxies used in Photo Tourism and the related Photosynth system from Microsoft result in non-photorealistic transitions reminiscent of visual effects such as "page flips". Selecting a stable 3D axis for all the planes can reduce the amount of swimming and enhance the perception of 3D (Figure 14.4c) (Snavely, Garg *et al.* 2008). It is also possible to automatically detect objects in the scene that are seen from multiple views and create "orbits" of viewpoints around such objects. Furthermore, nearby images in both 3D position and viewing direction can be linked to create "virtual paths", which can then be used to navigate between arbitrary pairs of images, such as those you might take yourself while walking around a popular tourist site (Snavely, Garg *et al.* 2008). This idea

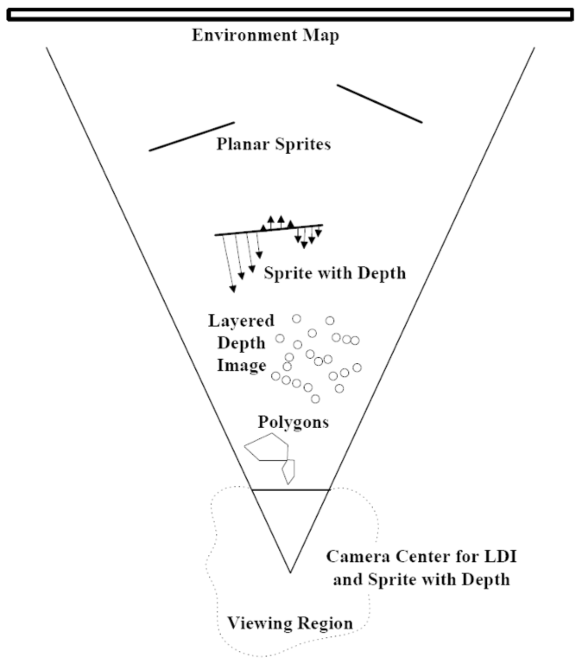

Figure 14.5 A variety of image-based rendering primitives, which can be used depending on the distance between the camera and the object of interest (Shade, Gortler *et al.* 1998) © 1998 ACM. Closer objects may require more detailed polygonal representations, while mid-level objects can use a layered depth image (LDI), and far-away objects can use sprites (potentially with depth) and environment maps.

has been further developed and released as a feature on Google Maps called Photo Tours (Kushal, Self *et al.* 2012).[3] The quality of such synthesized virtual views has become so accurate that Shan, Adams *et al.* (2013) propose a *visual Turing test* to distinguish between synthetic and real images. Waechter, Beljan *et al.* (2017) produce higher-resolution quality assessments of image-based modeling and rendering system using what they call *virtual rephotography*. Further improvements can be obtained using even more recent *neural rendering* techniques (Hedman, Philip *et al.* 2018; Meshry, Goldman *et al.* 2019; Li, Xian *et al.* 2020), which we discuss in Section 14.6.

The spatial matching of image features and regions performed by Photo Tourism can also be used to infer more information from large image collections. For example, Simon, Snavely, and Seitz (2007) show how the match graph between images of popular tourist sites can be used to find the most *iconic* (commonly photographed) objects in the collection, along with their related tags. In follow-on work, Simon and Seitz (2008) show how such tags can be propagated to sub-regions of each image, using an analysis of which 3D points appear in the central portions of photographs. Extensions of these techniques to *all* of the world's images, including the use of GPS tags where available, have been investigated as well (Li, Wu *et al.* 2008; Quack, Leibe, and Van Gool 2008; Crandall, Backstrom *et al.* 2009; Li, Crandall, and Huttenlocher 2009; Zheng, Zhao *et al.* 2009; Raguram, Wu *et al.* 2011).

[3]https://maps.googleblog.com/2012/04/visit-global-landmarks-with-photo-tours.html

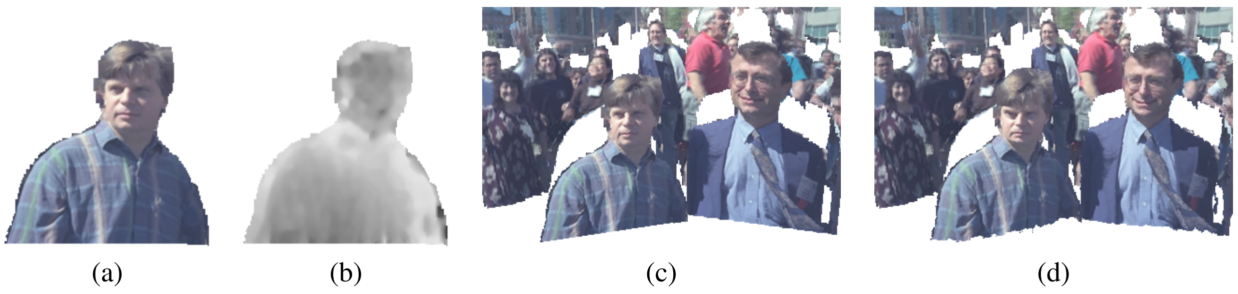

Figure 14.6 Sprites with depth (Shade, Gortler *et al.* 1998) © 1998 ACM: (a) alpha-matted color sprite; (b) corresponding relative depth or parallax; (c) rendering without relative depth; (d) rendering with depth (note the curved object boundaries).

14.2 Layered depth images

Traditional view interpolation techniques associate a single depth map with each source or reference image. Unfortunately, when such a depth map is warped to a novel view, holes and cracks inevitably appear behind the foreground objects. One way to alleviate this problem is to keep several depth and color values (*depth pixels*) at every pixel in a reference image (or, at least for pixels near foreground–background transitions) (Figure 14.5). The resulting data structure, which is called a *layered depth image* (LDI), can be used to render new views using a back-to-front forward warping (splatting) algorithm (Shade, Gortler *et al.* 1998).

14.2.1 Impostors, sprites, and layers

An alternative to keeping lists of color-depth values at each pixel, as is done in the LDI, is to organize objects into different *layers* or *sprites*. The term sprite originates in the computer game industry, where it is used to designate flat animated characters in games such as Pac-Man or Mario Bros. When put into a 3D setting, such objects are often called *impostors*, because they use a piece of flat, alpha-matted geometry to represent simplified versions of 3D objects that are far away from the camera (Shade, Lischinski *et al.* 1996; Lengyel and Snyder 1997; Torborg and Kajiya 1996). In computer vision, such representations are usually called *layers* (Wang and Adelson 1994; Baker, Szeliski, and Anandan 1998; Torr, Szeliski, and Anandan 1999; Birchfield, Natarajan, and Tomasi 2007). Section 9.4.2 discusses the topics of transparent layers and reflections, which occur on specular and transparent surfaces such as glass.

While flat layers can often serve as an adequate representation of geometry and appearance for far-away objects, better geometric fidelity can be achieved by also modeling the per-pixel offsets relative to a base plane, as shown in Figures 14.5 and 14.6a–b. Such representations are called *plane plus parallax* in the computer vision literature (Kumar, Anandan, and Hanna 1994; Sawhney 1994; Szeliski and Coughlan 1997; Baker, Szeliski, and Anandan 1998), as discussed in Section 9.4 (Figure 9.14). In addition to fully automated stereo techniques, it is also possible to paint in depth layers (Kang 1998; Oh, Chen *et al.* 2001; Shum, Sun *et al.* 2004) or to infer their 3D structure from monocular image cues (Sections 6.4.4 and 12.8) (Hoiem, Efros, and Hebert 2005b; Saxena, Sun, and Ng 2009).

How can we render a sprite with depth from a novel viewpoint? One possibility, as with a regular depth map, is to just forward warp each pixel to its new location, which can cause aliasing and cracks. A better way, which we have already mentioned in Section 3.6.2, is to first warp the depth (or (u, v) displacement) map to the novel view, fill in the cracks, and then use higher-quality

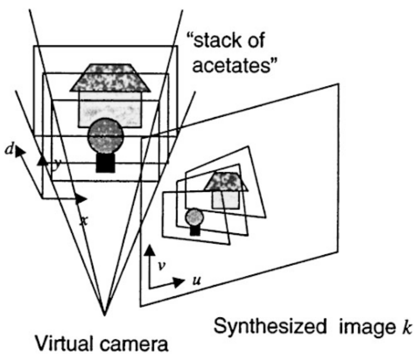

(a)

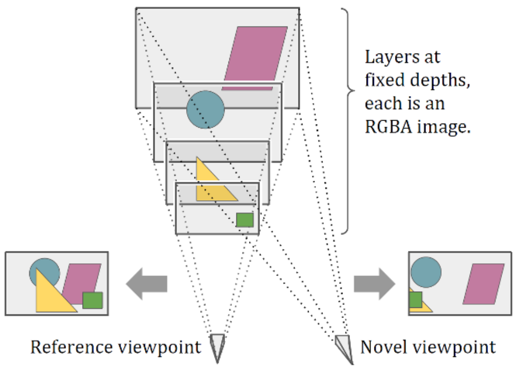

(b)

Figure 14.7 Finely sliced fronto-parallel layers: (a) stack of acetates (Szeliski and Golland 1999) © 1999 Springer and (b) multiplane images (Zhou, Tucker *et al.* 2018) © 2018 ACM. These representations (which are equivalent) consist of a set of fronto-parallel planes at fixed depths from a reference camera coordinate frame, with each plane encoding an RGB image and an alpha map that capture the scene appearance at the corresponding depth.

inverse warping to resample the color image (Shade, Gortler *et al.* 1998). Figure 14.6d shows the results of applying such a two-pass rendering algorithm. From this still image, you can appreciate that the foreground sprites look more rounded; however, to fully appreciate the improvement in realism, you would have to look at the actual animated sequence.

Sprites with depth can also be rendered using conventional graphics hardware, as described in (Zitnick, Kang *et al.* 2004). Rogmans, Lu *et al.* (2009) describe GPU implementations of both real-time stereo matching and real-time forward and inverse rendering algorithms.

An alternative to constructing a small number of layers is to discretize the viewing frustum subtending a layered depth image into a large number of fronto-parallel planes, each of which contains RGBA values (Szeliski and Golland 1999), as shown in Figure 14.7. This is the same spatial representation we presented in Section 12.1.2 and Figure 12.6 on *plane sweep* approaches to stereo, except that here it is being used to represent a colored 3D scene instead of accumulating a matching cost volume. This representation is essentially a perspective variant of a volumetric representation containing RGB color and α opacity values (Sections 13.2.1 and 13.5).

This representation was recently rediscovered and now goes under the popular name of *multiplane images (MPI)* (Zhou, Tucker *et al.* 2018). Figure 14.8 shows an MPI representation derived from a stereo image pair along with a novel synthesized view. MPIs are easier to derive from pairs or collections of stereo images than true (minimal) layered representations because there is a 1:1 correspondence between pixels (actually, voxels) in a plane sweep cost volume (Figure 12.5) and an MPI. However, they are not as compact and can lead to tearing artifacts once the viewpoint exceeds a certain range. (We will talk about using inpainting to mitigate such holes in image-based representations in Section 14.2.2). MPIs are also related to the *soft 3D* volumetric representation proposed earlier by Penner and Zhang (2017).

Since their initial development for novel view extrapolation, i.e., "stereo magnification" (Zhou, Tucker *et al.* 2018), MPIs have found a wide range of applications in image-based rendering, including extension to multiple input images and faster inference (Flynn, Broxton *et al.* 2019), CNN refinement and better inpainting (Srinivasan, Tucker *et al.* 2019), interpolating between collections of MPIs (Mildenhall, Srinivasan *et al.* 2019), and large view extrapolations (Choi, Gallo *et al.* 2019). The planar MPI structure has also been generalized to curved surfaces for representing partial or

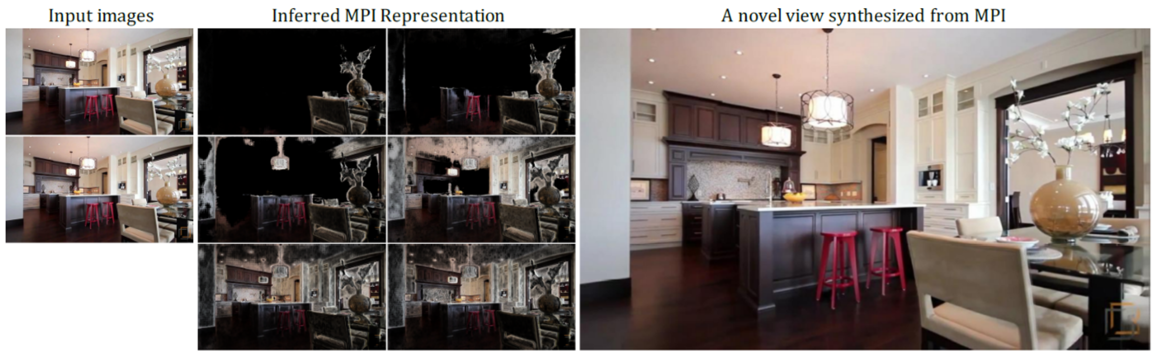
Input images
Inferred MPI Representation
A novel view synthesized from MPI

Figure 14.8 MPI representation constructed from a stereo pair of color images, along with a novel view reconstructed from the MPI (Zhou, Tucker *et al.* 2018) © 2018 ACM. Note how the planes slice the 3D scene into thin layers, each of which has colors and full or partial opacities in only a small region.

complete 3D panoramas (Broxton, Flynn *et al.* 2020; Attal, Ling *et al.* 2020; Lin, Xu *et al.* 2020).[4]

Another important application of layers is in the modeling of reflections. When the reflector (e.g., a glass pane) is planar, the reflection forms a *virtual image*, which can be modeled as a separate layer (Section 9.4.2 and Figures 9.16–9.17), so long as *additive* (instead of *over*) compositing is used to combine the reflected and transmitted images (Szeliski, Avidan, and Anandan 2000; Sinha, Kopf *et al.* 2012; Kopf, Langguth *et al.* 2013). Figure 14.9 shows an example of a two-layer decomposition reconstructed from a short video clip, which can be re-rendered from novel views by adding warped versions of the two layers (each of which has its own depth map). When the reflective surface is curved, a quasi-stable virtual image may still be available, although this depends on the local variations in principal curvatures (Swaminathan, Kang *et al.* 2002; Criminisi, Kang *et al.* 2005). The modeling of reflections is one of the advantages attributed to layered representations such as MPIs (Zhou, Tucker *et al.* 2018; Broxton, Flynn *et al.* 2020), although in these papers over compositing is still used, which results in plausible but not physically correct renderings.

14.2.2 *Application*: 3D photography

The desire to capture and view photographs of the world in 3D prompted the development of stereo cameras and viewers in the mid-1800s (Luo, Kong *et al.* 2020) and more recently the popularity of 3D movies.[5] It has also underpinned much of the research in 3D shape and appearance capture and modeling we studied in the previous chapter and more specifically Section 13.7.2. Until recently, however, while the required multiple images could be captured with hand-held cameras (Pollefeys, Van Gool *et al.* 2004; Snavely, Seitz, and Szeliski 2006), desktop or laptop computers were required to process and interactively view the images.

The ability to capture, construct, and widely share such 3D models has dramatically increased in the last few years and now goes under the name of *3D photography*. Hedman, Alsisan *et al.* (2017) describe their *Casual 3D Photography* system, which takes a sequence of overlapping images taken from a moving camera and then uses a combination of structure from motion, multi-view stereo, and 3D image warping and stitching to construct two-layer partial panoramas that can be viewed on a computer, as shown in Figure 14.10. The Instant 3D system of Hedman and Kopf (2018) builds a

[4]Exploring the interactive 3D videos on the authors' websites, e.g., https://augmentedperception.github.io/deepviewvideo, is a good way to get a sense of this new medium.

[5]It is interesting to note, however, that for now (at least), in-home 3D TV sets have failed to take off.

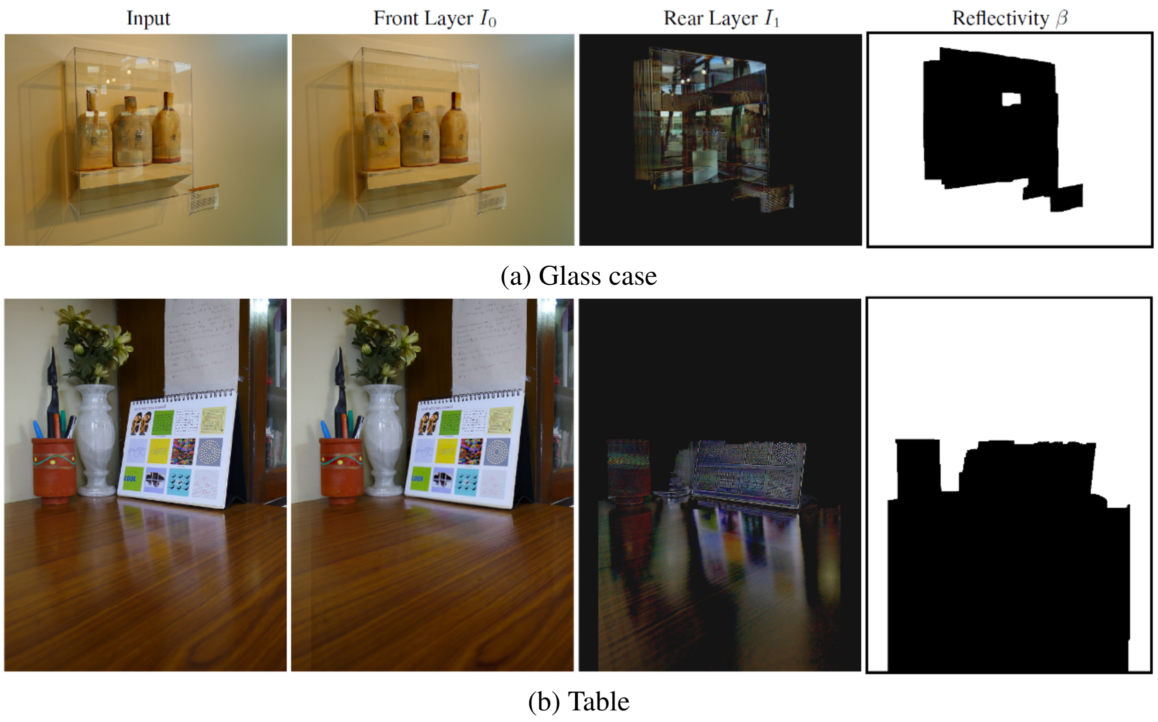

Figure 14.9 Image-based rendering of scenes with reflections using multiple additive layers (Sinha, Kopf *et al.* 2012) © 2012 ACM. The left column shows an image from the input sequence and the next two columns show the two separated layers (transmitted and reflected light). The last column is an estimate of which portions of the scene are reflective. As you can see, stray bits of reflections sometimes cling to the transmitted light layer. Note how in the table, the amount of reflected light (gloss) decreases towards the bottom of the image because of Fresnel reflection.

similar system, but starts with the depth images available from newer dual-camera smartphones to significantly speed up the process. Note, however, that the individual depth images are not *metric*, i.e., related to true depth with a single global scalar transformation, so must be deformably warped before being stitched together. A *texture atlas* is then constructed to compactly store the pixel color values while also supporting multiple layers.

While these systems produce beautiful wide 3D images that can create a true sense of immersion ("being there"), much more practical and fast solutions can be constructed using a single depth image. Kopf, Alsisan *et al.* (2019) describe their phone-based system, which takes a single dual-lens photograph with its estimated depth map and constructs a multi-layer 3D photograph with occluded pixels being *inpainted* from nearby background pixels (see Section 10.5.1 and Shih, Su *et al.* 2020).[6] To remove the requirement for depth maps being associated with the input images Kopf, Matzen *et al.* (2020) use a monocular depth inference network (Section 12.8) to estimate the depth, thereby enabling 3D photos to be produced from any photograph in a phone's camera roll, or even from historical photographs, as shown in Figure 14.10c.[7] When historic stereographs are available, these can be used to create even more accurate 3D photographs, as shown by Luo, Kong *et al.* (2020). It is also possible to create a "3D Ken Burns" effect, i.e., small looming video clips, from regular images

[6]Facebook rolled out 3D photographs for the iPhone in October 2018, https://facebook360.fb.com/2018/10/11/3d-photos-now-rolling-out-on-facebook-and-in-vr, along with the ability to post and interactively view the photos.

[7]In February 2020, Facebook released the ability to use regular photos, https://ai.facebook.com/blog/powered-by-ai-turning-any-2d-photo-into-3d-using-convolutional-neural-nets.

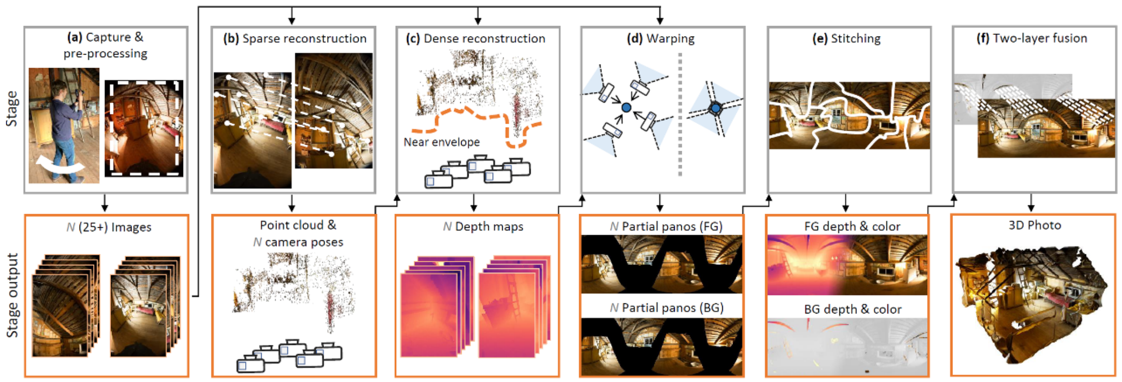

(a) Casual 3D Photography

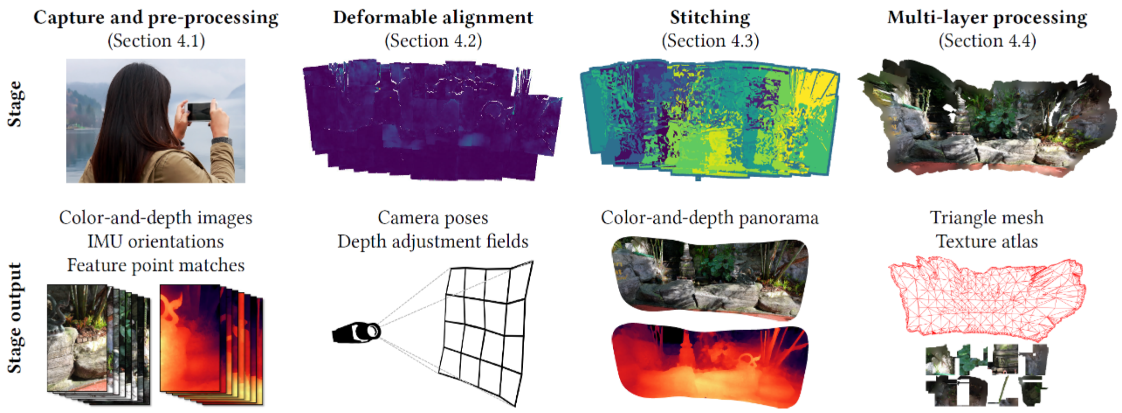

(b) Instant 3D Photography

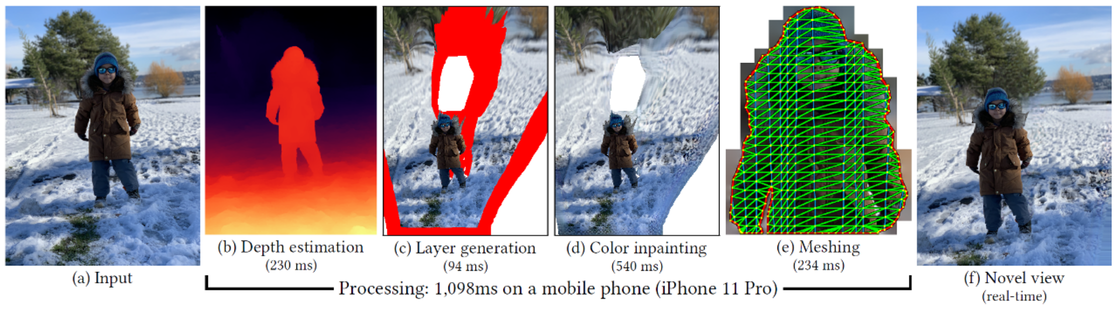
(a) Input
(b) Depth estimation (230 ms)
(c) Layer generation (94 ms)
(d) Color inpainting (540 ms)
(e) Meshing (234 ms)
(f) Novel view (real-time)
Processing: 1,098ms on a mobile phone (iPhone 11 Pro)

(c) One Shot 3D Photography

Figure 14.10 Systems for capturing and modeling 3D scenes from handheld photographs. (a) Casual 3D Photography takes a series of overlapping images and constructs per-image depth maps, which are then warped and blended together into a two-layer representation (Hedman, Alsisan *et al.* 2017) © 2017 ACM. (b) Instant 3D Photography starts with the depth maps produced by a dual-lens smartphone and warps and registers the depth maps to create a similar representation with far less computation (Hedman and Kopf 2018) © 2018 ACM. (c) One Shot 3D Photography starts with a single photo, performs monocular depth estimation, layer construction and inpainting, and mesh and atlas generation, enabling phone-based reconstruction and interactive viewing (Kopf, Matzen *et al.* 2020) © 2020 ACM.

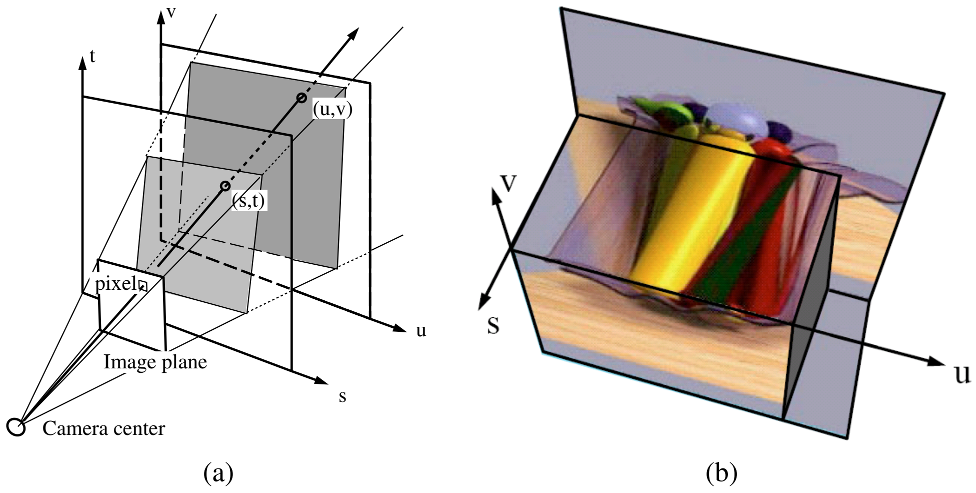

Figure 14.11 The Lumigraph (Gortler, Grzeszczuk *et al.* 1996) © 1996 ACM: (a) a ray is represented by its 4D two-plane parameters (s, t) and (u, v); (b) a slice through the 3D light field subset (u, v, s).

using monocular depth inference (Niklaus, Mai *et al.* 2019).[8]

14.3 Light fields and Lumigraphs

While image-based rendering approaches can synthesize scene renderings from novel viewpoints, they raise the following more general question:

> *Is is possible to capture and render the appearance of a scene from all possible viewpoints and, if so, what is the complexity of the resulting structure?*

Let us assume that we are looking at a static scene, i.e., one where the objects and illuminants are fixed, and only the observer is moving around. Under these conditions, we can describe each image by the location and orientation of the virtual camera (6 dof) as well as its intrinsics (e.g., its focal length). However, if we capture a two-dimensional *spherical* image around each possible camera location, we can re-render any view from this information.[9] Thus, taking the cross-product of the three-dimensional space of camera positions with the 2D space of spherical images, we obtain the 5D *plenoptic function* of Adelson and Bergen (1991), which forms the basis of the image-based rendering system of McMillan and Bishop (1995).

Notice, however, that when there is no light dispersion in the scene, i.e., no smoke or fog, all the coincident rays along a portion of free space (between solid or refractive objects) have the same color value. Under these conditions, we can reduce the 5D plenoptic function to the 4D *light field* of all possible rays (Gortler, Grzeszczuk *et al.* 1996; Levoy and Hanrahan 1996; Levoy 2006).[10]

To make the parameterization of this 4D function simpler, let us put two planes in the 3D scene roughly bounding the area of interest, as shown in Figure 14.11a. Any light ray terminating at a camera that lives in front of the st plane (assuming that this space is empty) passes through the two

[8] Google released a similar feature called Cinematic photos https://blog.google/products/photos/new-cinematic-photos-and-more-ways-relive-your-memories.

[9] As we are counting dimensions, we ignore for now any sampling or resolution issues.

[10] Levoy and Hanrahan (1996) borrowed the term *light field* from a paper by Gershun (1939). Another name for this representation is the *photic field* (Moon and Spencer 1981).

planes at (s, t) and (u, v) and can be described by its 4D coordinate (s, t, u, v). This diagram (and parameterization) can be interpreted as describing a family of cameras living on the st plane with their image planes being the uv plane. The uv plane can be placed at infinity, which corresponds to all the virtual cameras looking in the same direction.

In practice, if the planes are of finite extent, the finite *light slab* $L(s, t, u, v)$ can be used to generate any synthetic view that a camera would see through a (finite) *viewport* in the st plane with a view frustum that wholly intersects the far uv plane. To enable the camera to move all the way around an object, the 3D space surrounding the object can be split into multiple domains, each with its own light slab parameterization. Conversely, if the camera is moving inside a bounded volume of free space looking outward, multiple cube faces surrounding the camera can be used as (s, t) planes.

Thinking about 4D spaces is difficult, so let us drop our visualization by one dimension. If we fix the row value t and constrain our camera to move along the s axis while looking at the uv plane, we can stack all of the stabilized images the camera sees to get the (u, v, s) *epipolar volume*, which we discussed in Section 12.7. A "horizontal" cross-section through this volume is the well-known *epipolar plane image* (Bolles, Baker, and Marimont 1987), which is the us slice shown in Figure 14.11b.

As you can see in this slice, each color pixel moves along a linear track whose slope is related to its depth (parallax) from the uv plane. (Pixels exactly on the uv plane appear "vertical", i.e., they do not move as the camera moves along s.) Furthermore, pixel tracks occlude one another as their corresponding 3D surface elements occlude. Translucent pixels, however, composite *over* background pixels (Section 3.1.3 (3.8)) rather than occluding them. Thus, we can think of adjacent pixels sharing a similar planar geometry as *EPI strips* or *EPI tubes* (Criminisi, Kang *et al.* 2005). 3D lightfields taken from a camera slowly moving through a static scene can be an excellent source for high-accuracy 3D reconstruction, as demonstrated in the papers by Kim, Zimmer *et al.* (2013), Yücer, Kim *et al.* (2016), and Yücer, Sorkine-Hornung *et al.* (2016).

The equations mapping from pixels (x, y) in a virtual camera and the corresponding (s, t, u, v) coordinates are relatively straightforward to derive and are sketched out in Exercise 14.7. It is also possible to show that the set of pixels corresponding to a regular orthographic or perspective camera, i.e., one that has a linear projective relationship between 3D points and (x, y) pixels (2.63), lie along a two-dimensional hyperplane in the (s, t, u, v) light field (Exercise 14.7).

While a light field can be used to render a complex 3D scene from novel viewpoints, a much better rendering (with less ghosting) can be obtained if something is known about its 3D geometry. The Lumigraph system of Gortler, Grzeszczuk *et al.* (1996) extends the basic light field rendering approach by taking into account the 3D location of surface points corresponding to each 3D ray.

Consider the ray (s, u) corresponding to the dashed line in Figure 14.12, which intersects the object's surface at a distance z from the uv plane. When we look up the pixel's color in camera s_i (assuming that the light field is discretely sampled on a regular 4D (s, t, u, v) grid), the actual pixel coordinate is u', instead of the original u value specified by the (s, u) ray. Similarly, for camera s_{i+1} (where $s_i \leq s \leq s_{i+1}$), pixel address u'' is used. Thus, instead of using quadri-linear interpolation of the nearest sampled (s, t, u, v) values around a given ray to determine its color, the (u, v) values are modified for each discrete (s_i, t_i) camera.

Figure 14.12 also shows the same reasoning in *ray space*. Here, the original continuous-valued (s, u) ray is represented by a triangle and the nearby sampled discrete values are shown as circles. Instead of just blending the four nearest samples, as would be indicated by the vertical and horizontal dashed lines, the modified (s_i, u') and (s_{i+1}, u'') values are sampled instead and their values are then blended.

The resulting rendering system produces images of much better quality than a proxy-free light

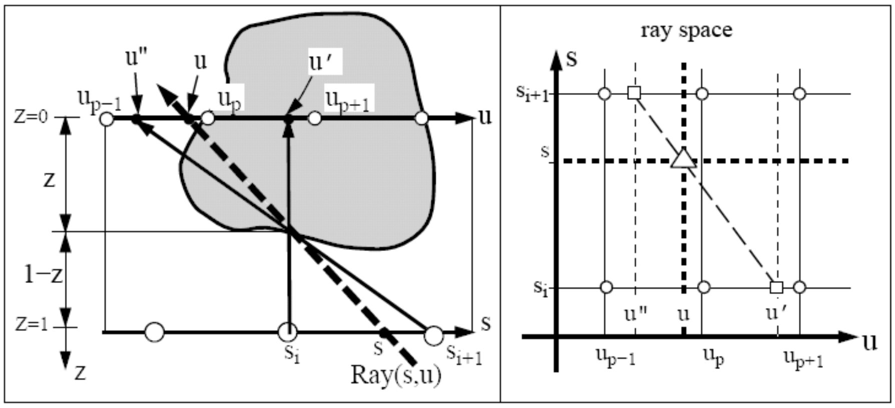

Figure 14.12 Depth compensation in the Lumigraph (Gortler, Grzeszczuk *et al.* 1996) © 1996 ACM. To resample the (s, u) dashed light ray, the u parameter corresponding to each discrete s_i camera location is modified according to the out-of-plane depth z to yield new coordinates u and u'; in (u, s) ray space, the original sample ($\triangle$) is resampled from the (s_i, u') and (s_{i+1}, u'') samples, which are themselves linear blends of their adjacent ($\circ$) samples.

field and is the method of choice whenever 3D geometry can be inferred. In subsequent work, Isaksen, McMillan, and Gortler (2000) show how a planar proxy for the scene, which is a simpler 3D model, can be used to simplify the resampling equations. They also describe how to create synthetic aperture photos, which mimic what might be seen by a wide-aperture lens, by blending more nearby samples (Levoy and Hanrahan 1996). A similar approach can be used to re-focus images taken with a plenoptic (microlens array) camera (Ng, Levoy *et al.* 2005; Ng 2005) or a light field microscope (Levoy, Ng *et al.* 2006). It can also be used to see through obstacles, using extremely large synthetic apertures focused on a background that can blur out foreground objects and make them appear translucent (Wilburn, Joshi *et al.* 2005; Vaish, Szeliski *et al.* 2006).

Now that we understand how to render new images from a light field, how do we go about capturing such datasets? One answer is to move a calibrated camera with a motion control rig or *gantry*.[11] Another approach is to take handheld photographs and to determine the pose and intrinsic calibration of each image using either a calibrated stage or structure from motion. In this case, the images need to be *rebinned* into a regular 4D (s, t, u, v) space before they can be used for rendering (Gortler, Grzeszczuk *et al.* 1996). Alternatively, the original images can be used directly using a process called the *unstructured Lumigraph*, which we describe below.

Because of the large number of images involved, light fields and Lumigraphs can be quite voluminous to store and transmit. Fortunately, as you can tell from Figure 14.11b, there is a tremendous amount of redundancy (coherence) in a light field, which can be made even more explicit by first computing a 3D model, as in the Lumigraph. A number of techniques have been developed to compress and progressively transmit such representations (Gortler, Grzeszczuk *et al.* 1996; Levoy and Hanrahan 1996; Rademacher and Bishop 1998; Magnor and Girod 2000; Wood, Azuma *et al.* 2000; Shum, Kang, and Chan 2003; Magnor, Ramanathan, and Girod 2003; Zhang and Chen 2004; Shum, Chan, and Kang 2007).

Since the original burst of research on lightfields in the mid-1990 and early 2000s, better tech-

[11] See http://lightfield.stanford.edu/acq.html for a description of some of the gantries and camera arrays built at the Stanford Computer Graphics Laboratory (Wilburn, Joshi *et al.* 2005). A more recent dataset was created by Honauer, Johannsen *et al.* (2016) and is available at https://lightfield-analysis.uni-konstanz.de Both websites provide light field datasets that are a great source of research and project material.

niques continue to be developed for analyzing and rendering such images. Some representative papers and datasets from the last decade include Wanner and Goldluecke (2014), Honauer, Johannsen *et al.* (2016), Kalantari, Wang, and Ramamoorthi (2016), Wu, Masia *et al.* (2017), and Shin, Jeon *et al.* (2018).

14.3.1 Unstructured Lumigraph

When the images in a Lumigraph are acquired in an unstructured (irregular) manner, it can be counterproductive to resample the resulting light rays into a regularly binned (s, t, u, v) data structure. This is both because resampling always introduces a certain amount of aliasing and because the resulting gridded light field can be populated very sparsely or irregularly.

The alternative is to render directly from the acquired images, by finding for each light ray in a virtual camera the closest pixels in the original images. The *unstructured Lumigraph* rendering (ULR) system of Buehler, Bosse *et al.* (2001) describes how to select such pixels by combining a number of fidelity criteria, including *epipole consistency* (distance of rays to a source camera's center), *angular deviation* (similar incidence direction on the surface), *resolution* (similar sampling density along the surface), *continuity* (to nearby pixels), and *consistency* (along the ray). These criteria can all be combined to determine a weighting function between each virtual camera's pixel and a number of candidate input cameras from which it can draw colors. To make the algorithm more efficient, the computations are performed by discretizing the virtual camera's image plane using a regular grid overlaid with the polyhedral object mesh model and the input camera centers of projection and interpolating the weighting functions between vertices.

The unstructured Lumigraph generalizes previous work in both image-based rendering and light field rendering. When the input cameras are gridded, the ULR behaves the same way as regular Lumigraph rendering. When fewer cameras are available but the geometry is accurate, the algorithm behaves similarly to view-dependent texture mapping (Section 14.1.1). If RGB-D depth images are available, these can be fused into lower-resolution proxies that can be combined with higher-resolution source images at rendering time (Hedman, Ritschel *et al.* 2016). And while the original ULR paper uses manually constructed rules for determining pixel weights, it is also possible to learn such blending weights using a deep neural network (Hedman, Philip *et al.* 2018; Riegler and Koltun 2020a).

14.3.2 Surface light fields

Of course, using a two-plane parameterization for a light field is not the only possible choice. (It is the one usually presented first, as the projection equations and visualizations are the easiest to draw and understand.) As we mentioned on the topic of light field compression, if we know the 3D shape of the object or scene whose light field is being modeled, we can effectively compress the field because nearby rays emanating from nearby surface elements have similar color values.

In fact, if the object is totally diffuse, ignoring occlusions, which can be handled using 3D graphics algorithms or z-buffering, all rays passing through a given surface point will have the same color value. Hence, the light field "collapses" to the usual 2D texture-map defined over an object's surface. Conversely, if the surface is totally specular (e.g., mirrored), each surface point reflects a miniature copy of the environment surrounding that point. In the absence of inter-reflections (e.g., a convex object in a large open space), each surface point simply reflects the far-field *environment map* (Section 2.2.1), which again is two-dimensional. Therefore, is seems that re-parameterizing the 4D light field to lie on the object's surface can be extremely beneficial.

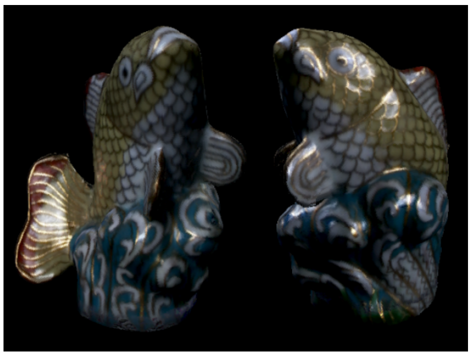
(a)

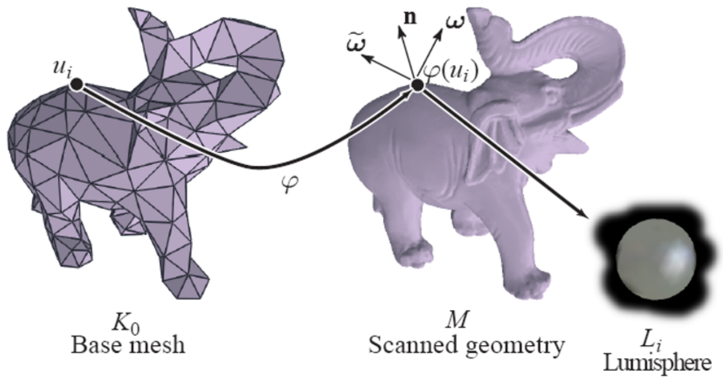

(b)

Figure 14.13 Surface light fields (Wood, Azuma *et al.* 2000) © 2000 ACM: (a) example of a highly specular object with strong inter-reflections; (b) the surface light field stores the light emanating from each surface point in all visible directions as a "Lumisphere".

These observations underlie the *surface light field* representation introduced by Wood, Azuma *et al.* (2000). In their system, an accurate 3D model is built of the object being represented. Then the *Lumisphere* of all rays emanating from each surface point is estimated or captured (Figure 14.13). Nearby Lumispheres will be highly correlated and hence amenable to both compression and manipulation.

To estimate the diffuse component of each Lumisphere, a median filtering over all visible exiting directions is first performed for each channel. Once this has been subtracted from the Lumisphere, the remaining values, which should consist mostly of the specular components, are *reflected* around the local surface normal (2.90), which turns each Lumisphere into a copy of the local environment around that point. Nearby Lumispheres can then be compressed using predictive coding, vector quantization, or principal component analysis.

The decomposition into a diffuse and specular component can also be used to perform editing or manipulation operations, such as re-painting the surface, changing the specular component of the reflection (e.g., by blurring or sharpening the specular Lumispheres), or even geometrically deforming the object while preserving detailed surface appearance.

In more recent work, Park, Newcombe, and Seitz (2018) use an RGB-D camera to acquire a 3D model and its diffuse reflectance layer using min compositing and iteratively reweighted least squares, as discussed in Section 9.4.2. They then estimate a simple piecewise-constant BRDF model to account for the specular components. In their follow-on Seeing the World in a Bag of Chips paper, Park, Holynski, and Seitz (2020) also estimate the *specular reflectance map*, which is a convolution of the environment map with the object's specular BRDF. Additional techniques to estimate spatially varying BRDFs are discussed in Section 13.7.1.

In summary, surface light fields are a good representation to add realism to scanned 3D object models by modeling their specular properties, thus avoiding the "cardboard" (matte) appearance of such models when their reflections are ignored. For larger scenes, especially those containing large planar reflectors such as glass windows or glossy tables, modeling the reflections as separate layers, as discussed in Sections 9.4.2 and 14.2.1, or as true mirror surfaces (Whelan, Goesele *et al.* 2018), may be more appropriate.

14.3.3 *Application*: Concentric mosaics

A useful and simple version of light field rendering is a panoramic image with parallax, i.e., a video or series of photographs taken from a camera swinging in front of some rotation point. Such panoramas can be captured by placing a camera on a boom on a tripod, or even more simply, by holding a camera at arm's length while rotating your body around a fixed axis.

The resulting set of images can be thought of as a *concentric mosaic* (Shum and He 1999; Shum, Wang *et al.* 2002) or a *layered depth panorama* (Zheng, Kang *et al.* 2007). The term "concentric mosaic" comes from a particular structure that can be used to re-bin all of the sampled rays, essentially associating each column of pixels with the "radius" of the concentric circle to which it is tangent (Ishiguro, Yamamoto, and Tsuji 1992; Shum and He 1999; Peleg, Ben-Ezra, and Pritch 2001).

Rendering from such data structures is fast and straightforward. If we assume that the scene is far enough away, for any virtual camera location, we can associate each column of pixels in the virtual camera with the nearest column of pixels in the input image set. (For a regularly captured set of images, this computation can be performed analytically.) If we have some rough knowledge of the depth of such pixels, columns can be stretched vertically to compensate for the change in depth between the two cameras. If we have an even more detailed depth map (Peleg, Ben-Ezra, and Pritch 2001; Li, Shum *et al.* 2004; Zheng, Kang *et al.* 2007), we can perform pixel-by-pixel depth corrections.

While the virtual camera's motion is constrained to lie in the plane of the original cameras and within the radius of the original capture ring, the resulting experience can exhibit complex rendering phenomena, such as reflections and translucencies, which cannot be captured using a texture-mapped 3D model of the world. Exercise 14.10 has you construct a concentric mosaic rendering system from a series of hand-held photos or video.

While concentric mosaics are captured by moving the camera on a (roughly) circular arc, it is also possible to construct *manifold projections* (Peleg and Herman 1997), *multiple-center-of-projection images* (Rademacher and Bishop 1998), and *multi-perspective panoramas* (Román, Garg, and Levoy 2004; Román and Lensch 2006; Agarwala, Agrawala *et al.* 2006; Kopf, Chen *et al.* 2010), which we discussed briefly in Section 8.2.5.

14.3.4 *Application*: Synthetic re-focusing

In addition to the interactive viewing of captured scenes and objects, light field rendering can be used to add synthetic depth of field effects to photographs (Levoy 2006). In the computational photography chapter (Section 10.3.2), we mentioned how the depth estimates produced by modern dual-lens and/or dual-pixel smartphones can be used to synthetically blur photographs (Wadhwa, Garg *et al.* 2018; Garg, Wadhwa *et al.* 2019; Zhang, Wadhwa *et al.* 2020).

When larger numbers of input images are available, e.g., when using microlens arrays, the images can be shifted and combined to simulate the effects of a larger aperture lens in what is known as *synthetic aperture photography* (Ng, Levoy *et al.* 2005; Ng 2005), which was the basis of the Lytro light field camera. Related ideas have been used for shallow depth of field in *light field microscopy* (Levoy, Chen *et al.* 2004; Levoy, Ng *et al.* 2006), obstruction removal (Wilburn, Joshi *et al.* 2005; Vaish, Szeliski *et al.* 2006; Xue, Rubinstein *et al.* 2015; Liu, Lai *et al.* 2020a), and *coded aperture photography* (Levin, Fergus *et al.* 2007; Zhou, Lin, and Nayar 2009).

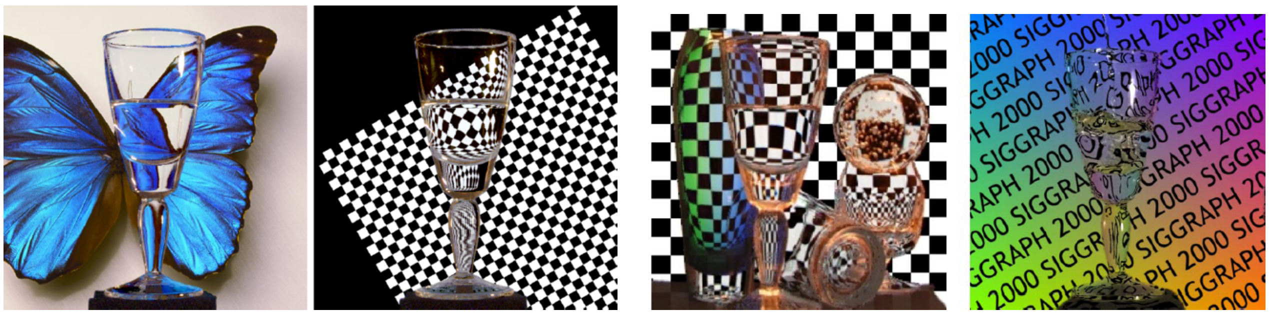

Figure 14.14 Environment mattes: (a–b) a refractive object can be placed in front of a series of backgrounds and their light patterns will be correctly refracted (Zongker, Werner *et al.* 1999) (c) multiple refractions can be handled using a Gaussian mixture model and (d) real-time mattes can be pulled using a single graded colored background (Chuang, Zongker *et al.* 2000) © 2000 ACM.

14.4 Environment mattes

So far in this chapter, we have dealt with view interpolation and light fields, which are techniques for modeling and rendering complex static scenes seen from different viewpoints.

What if, instead of moving around a virtual camera, we take a complex, refractive object, such as the water goblet shown in Figure 14.14, and place it in front of a new background? Instead of modeling the 4D space of rays emanating from a scene, we now need to model how each pixel in our view of this object refracts incident light coming from its environment.

What is the intrinsic dimensionality of such a representation and how do we go about capturing it? Let us assume that if we trace a light ray from the camera at pixel (x, y) toward the object, it is reflected or refracted back out toward its environment at an angle (ϕ, θ). If we assume that other objects and illuminants are sufficiently distant (the same assumption we made for surface light fields in Section 14.3.2), this 4D mapping $(x, y) \rightarrow (\phi, \theta)$ captures all the information between a refractive object and its environment. Zongker, Werner *et al.* (1999) call such a representation an *environment matte*, as it generalizes the process of object matting (Section 10.4) to not only cut and paste an object from one image into another but also take into account the subtle refractive or reflective interplay between the object and its environment.

Recall from Equations (3.8) and (10.29) that a foreground object can be represented by its pre-multiplied colors and opacities $(\alpha F, \alpha)$. Such a matte can then be composited onto a new background B using

$$C_i = \alpha_i F_i + (1 - \alpha_i) B_i, \tag{14.1}$$

where i is the pixel under consideration. In environment matting, we augment this equation with a reflective or refractive term to model indirect light paths between the environment and the camera. In the original work of Zongker, Werner *et al.* (1999), this indirect component I_i is modeled as

$$I_i = R_i \int A_i(\mathbf{x}) B(\mathbf{x}) d\mathbf{x}, \tag{14.2}$$

where A_i is the rectangular *area of support* for that pixel, R_i is the colored reflectance or transmittance (for colored glossy surfaces or glass), and $B(\mathbf{x})$ is the background (environment) image, which is integrated over the area $A_i(\mathbf{x})$. In follow-on work, Chuang, Zongker *et al.* (2000) use a superposition of oriented Gaussians,

$$I_i = \sum_j R_{ij} \int G_{ij}(\mathbf{x})B(\mathbf{x})d\mathbf{x}, \tag{14.3}$$

where each 2D Gaussian

$$G_{ij}(\mathbf{x}) = G_{\text{2D}}(\mathbf{x}; \mathbf{c}_{ij}, \sigma_{ij}, \theta_{ij}) \tag{14.4}$$

is modeled by its center $\mathbf{c}_{ij}$, unrotated widths $\sigma_{ij} = (\sigma^x_{ij}, \sigma^y_{ij})$, and orientation θ_{ij}.

Given a representation for an environment matte, how can we go about estimating it for a particular object? The trick is to place the object in front of a monitor (or surrounded by a set of monitors), where we can change the illumination patterns $B(\mathbf{x})$ and observe the value of each composite pixel C_i.[12]

As with traditional two-screen matting (Section 10.4.1), we can use a variety of solid colored backgrounds to estimate each pixel's foreground color $\alpha_i F_i$ and partial coverage (opacity) α_i. To estimate the area of support A_i in (14.2), Zongker, Werner *et al.* (1999) use a series of periodic horizontal and vertical solid stripes at different frequencies and phases, which is reminiscent of the structured light patterns used in active rangefinding (Section 13.2). For the more sophisticated Gaussian mixture model (14.3), Chuang, Zongker *et al.* (2000) sweep a series of narrow Gaussian stripes at four different orientations (horizontal, vertical, and two diagonals), which enables them to estimate multiple oriented Gaussian responses at each pixel.

Once an environment matte has been "pulled", it is then a simple matter to replace the background with a new image $B(\mathbf{x})$ to obtain a novel composite of the object placed in a different environment (Figure 14.14a–c). The use of multiple backgrounds during the matting process, however, precludes the use of this technique with dynamic scenes, e.g., water pouring into a glass (Figure 14.14d). In this case, a single graded color background can be used to estimate a single 2D monochromatic displacement for each pixel (Chuang, Zongker *et al.* 2000).

14.4.1 Higher-dimensional light fields

As you can tell from the preceding discussion, an environment matte in principle maps every pixel (x, y) into a 4D distribution over light rays and is, hence, a six-dimensional representation. (In practice, each 2D pixel's response is parameterized using a dozen or so parameters, e.g., $\{F, \alpha, B, R, A\}$, instead of a full mapping.) What if we want to model an object's refractive properties from every potential point of view? In this case, we need a mapping from every incoming 4D light ray to every potential exiting 4D light ray, which is an 8D representation. If we use the same trick as with surface light fields, we can parameterize each surface point by its 4D BRDF to reduce this mapping back down to 6D, but this loses the ability to handle multiple refractive paths.

If we want to handle dynamic light fields, we need to add another temporal dimension. (Wenger, Gardner *et al.* (2005) gives a nice example of a dynamic appearance and illumination acquisition system.) Similarly, if we want a continuous distribution over wavelengths, this becomes another dimension.

These examples illustrate how modeling the full complexity of a visual scene through sampling can be extremely expensive. Fortunately, constructing specialized models, which exploit knowledge about the physics of light transport along with the natural coherence of real-world objects, can make these problems more tractable.

[12] If we relax the assumption that the environment is distant, the monitor can be placed at several depths to estimate a depth-dependent mapping function (Zongker, Werner *et al.* 1999).

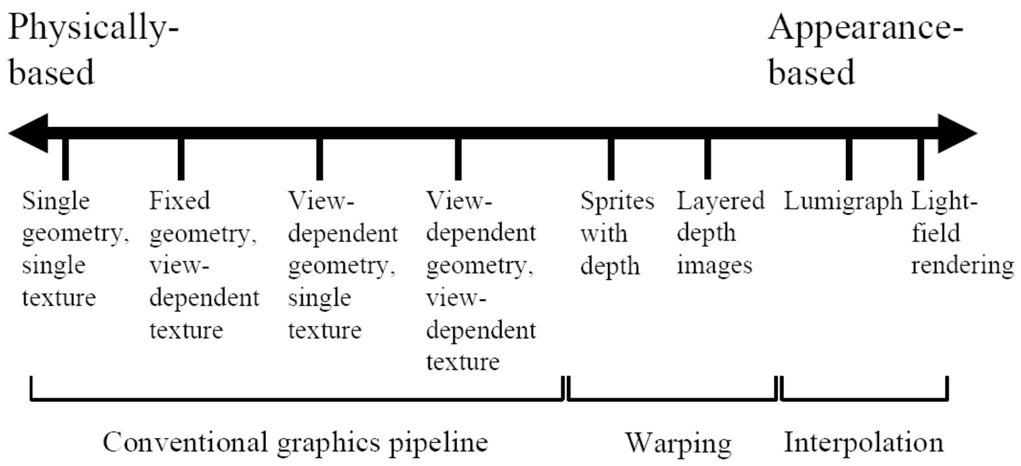
Physically-based
Appearance-based
Single geometry, single texture
Fixed geometry, view-dependent texture
View-dependent geometry, single texture
View-dependent geometry, view-dependent texture
Sprites with depth
Layered depth images
Lumigraph
Light-field rendering
Conventional graphics pipeline
Warping
Interpolation

Figure 14.15 The geometry–image continuum in image-based rendering (Kang, Szeliski, and Anandan 2000) © 2000 IEEE. Representations at the left of the spectrum use more detailed geometry and simpler image representations, while representations and algorithms on the right use more images and less geometry.

14.4.2 The modeling to rendering continuum

The image-based rendering representations and algorithms we have studied in this chapter span a continuum ranging from classic 3D texture-mapped models all the way to pure sampled ray-based representations such as light fields (Figure 14.15). Representations such as view-dependent texture maps and Lumigraphs still use a single global geometric model, but select the colors to map onto these surfaces from nearby images. View-dependent geometry, e.g., multiple depth maps, sidestep the need for coherent 3D geometry, and can sometimes better model local non-rigid effects such as specular motion (Swaminathan, Kang *et al.* 2002; Criminisi, Kang *et al.* 2005). Sprites with depth and layered depth images use image-based representations of both color and geometry and can be efficiently rendered using warping operations rather than 3D geometric rasterization.

The best choice of representation and rendering algorithm depends on both the quantity and quality of the input imagery as well as the intended application. When nearby views are being rendered, image-based representations capture more of the visual fidelity of the real world because they directly sample its appearance. On the other hand, if only a few input images are available or the image-based models need to be manipulated, e.g., to change their shape or appearance, more abstract 3D representations such as geometric and local reflection models are a better fit. As we continue to capture and manipulate increasingly larger quantities of visual data, research into these aspects of image-based modeling and rendering will continue to evolve.

14.5 Video-based rendering

As multiple images can be used to render new images or interactive experiences, can something similar be done with video? In fact, a fair amount of work has been done in the area of *video-based rendering* and *video-based animation*, two terms first introduced by Schödl, Szeliski *et al.* (2000) to denote the process of generating new video sequences from captured video footage. An early example of such work is Video Rewrite (Bregler, Covell, and Slaney 1997), in which archival video footage is "re-animated" by having actors say new utterances (Figure 14.16). More recently, the term video-based rendering has been used by some researchers to denote the creation of virtual

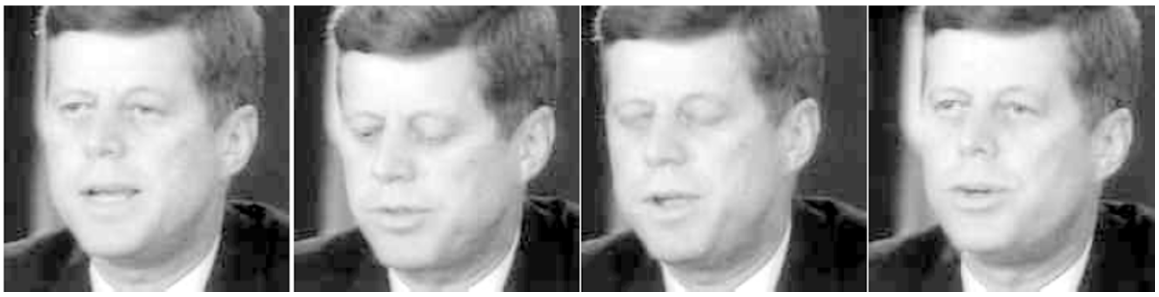

Figure 14.16 Video Rewrite (Bregler, Covell, and Slaney 1997) © 1997 ACM: the video frames are composed from bits and pieces of old video footage matched to a new audio track.

camera moves from a set of synchronized video cameras placed in a studio (Magnor 2005). (The terms *free-viewpoint video* and *3D video* are also sometimes used: see Section 14.5.4.)

In this section, we present a number of video-based rendering systems and applications. We start with *video-based animation* (Section 14.5.1), in which video footage is re-arranged or modified, e.g., in the capture and re-rendering of facial expressions. A special case of this is *video textures* (Section 14.5.2), in which source video is automatically cut into segments and re-looped to create infinitely long video animations. It is also possible to create such animations from still pictures or paintings, by segmenting the image into separately moving regions and animating them using stochastic motion fields (Section 14.5.3).

Next, we turn our attention to *3D video* (Section 14.5.4), in which multiple synchronized video cameras are used to film a scene from different directions. The source video frames can then be re-combined using image-based rendering techniques, such as view interpolation, to create virtual camera paths between the source cameras as part of a real-time viewing experience. Finally, we discuss capturing environments by driving or walking through them with panoramic video cameras to create interactive video-based walkthrough experiences (Section 14.5.5).

14.5.1 Video-based animation

As we mentioned above, an early example of video-based animation is Video Rewrite, in which frames from original video footage are rearranged to match them to novel spoken utterances, e.g., for movie dubbing (Figure 14.16). This is similar in spirit to the way that *concatenative speech synthesis* systems work (Taylor 2009).

In their system, Bregler, Covell, and Slaney (1997) first use speech recognition to extract phonemes from both the source video material and the novel audio stream. Phonemes are grouped into *triphones* (triplets of phonemes), as these better model the *coarticulation* effect present when people speak. Matching triphones are then found in the source footage and audio track. The mouth images corresponding to the selected video frames are then cut and pasted into the desired video footage being re-animated or dubbed, with appropriate geometric transformations to account for head motion. During the analysis phase, features corresponding to the lips, chin, and head are tracked using computer vision techniques. During synthesis, image morphing techniques are used to blend and stitch adjacent mouth shapes into a more coherent whole. In subsequent work, Ezzat, Geiger, and Poggio (2002) describe how to use a *multidimensional morphable model* (Section 13.6.2) combined with regularized trajectory synthesis to improve these results.

A more sophisticated version of this system, called *face transfer*, uses a novel source video, instead of just an audio track, to drive the animation of a previously captured video, i.e., to re-render a video of a talking head with the appropriate visual speech, expression, and head pose elements (Vlasic, Brand *et al.* 2005). This work is one of many *performance-driven animation* systems (Section 7.1.6), which are often used to animate 3D facial models (Figures 13.23–13.25). While traditional performance-driven animation systems use marker-based motion capture (Williams 1990; Litwinowicz and Williams 1994; Ma, Jones *et al.* 2008), video footage can now be used directly to control the animation (Buck, Finkelstein *et al.* 2000; Pighin, Szeliski, and Salesin 2002; Zhang, Snavely *et al.* 2004; Vlasic, Brand *et al.* 2005; Roble and Zafar 2009; Thies, Zollhofer *et al.* 2016; Thies, Zollhöfer *et al.* 2018; Zollhöfer, Thies *et al.* 2018; Fried, Tewari *et al.* 2019; Egger, Smith *et al.* 2020; Tewari, Fried *et al.* 2020). More details on related techniques can also be found in Section 13.6.3 on facial animation and Section 14.6 on neural rendering.

In addition to its most common application to facial animation, video-based animation can also be applied to whole body motion (Section 13.6.4), e.g., by matching the flow fields between two different source videos and using one to drive the other (Efros, Berg *et al.* 2003; Wang, Liu *et al.* 2018; Chan, Ginosar *et al.* 2019). Another approach to video-based rendering is to use flow or 3D modeling to *unwrap* surface textures into stabilized images, which can then be manipulated and re-rendered onto the original video (Pighin, Szeliski, and Salesin 2002; Rav-Acha, Kohli *et al.* 2008).

14.5.2 Video textures

Video-based animation is a powerful means of creating photo-realistic videos by re-purposing existing video footage to match some other desired activity or script. What if, instead of constructing a special animation or narrative, we simply want the video to continue playing in a plausible manner? For example, many websites use images or videos to highlight their destinations, e.g., to portray attractive beaches with surf and palm trees waving in the wind. Instead of using a static image or a video clip that has a discontinuity when it loops, can we transform the video clip into an infinite-length animation that plays forever?

This idea is the basis of *video textures*, in which a short video clip can be arbitrarily extended by re-arranging video frames while preserving visual continuity (Schödl, Szeliski *et al.* 2000). The basic problem in creating video textures is how to perform this re-arrangement without introducing visual artifacts. Can you think of how you might do this?

The simplest approach is to match frames by visual similarity (e.g., L_2 distance) and to jump between frames that appear similar. Unfortunately, if the motions in the two frames are different, a dramatic visual artifact will occur (the video will appear to "stutter"). For example, if we fail to match the motions of the clock pendulum in Figure 14.17a, it can suddenly change direction in mid-swing.

How can we extend our basic frame matching to also match motion? In principle, we could compute optical flow at each frame and match this. However, flow estimates are often unreliable (especially in textureless regions) and it is not clear how to weight the visual and motion similarities relative to each other. As an alternative, Schödl, Szeliski *et al.* (2000) suggest matching *triplets* or larger neighborhoods of adjacent video frames, much in the same way as Video Rewrite matches triphones. Once we have constructed an $n \times n$ similarity matrix between all video frames (where n is the number of frames), a simple finite impulse response (FIR) filtering of each match sequence can be used to emphasize subsequences that match well.

The results of this match computation gives us a *jump table* or, equivalently, a transition probability between any two frames in the original video. This is shown schematically as red arcs in Figure 14.17b, where the red bar indicates which video frame is currently being displayed, and arcs light up as a forward or backward transition is taken. We can view these transition probabilities as encoding the *hidden Markov model* (HMM) that underlies a stochastic video generation process.

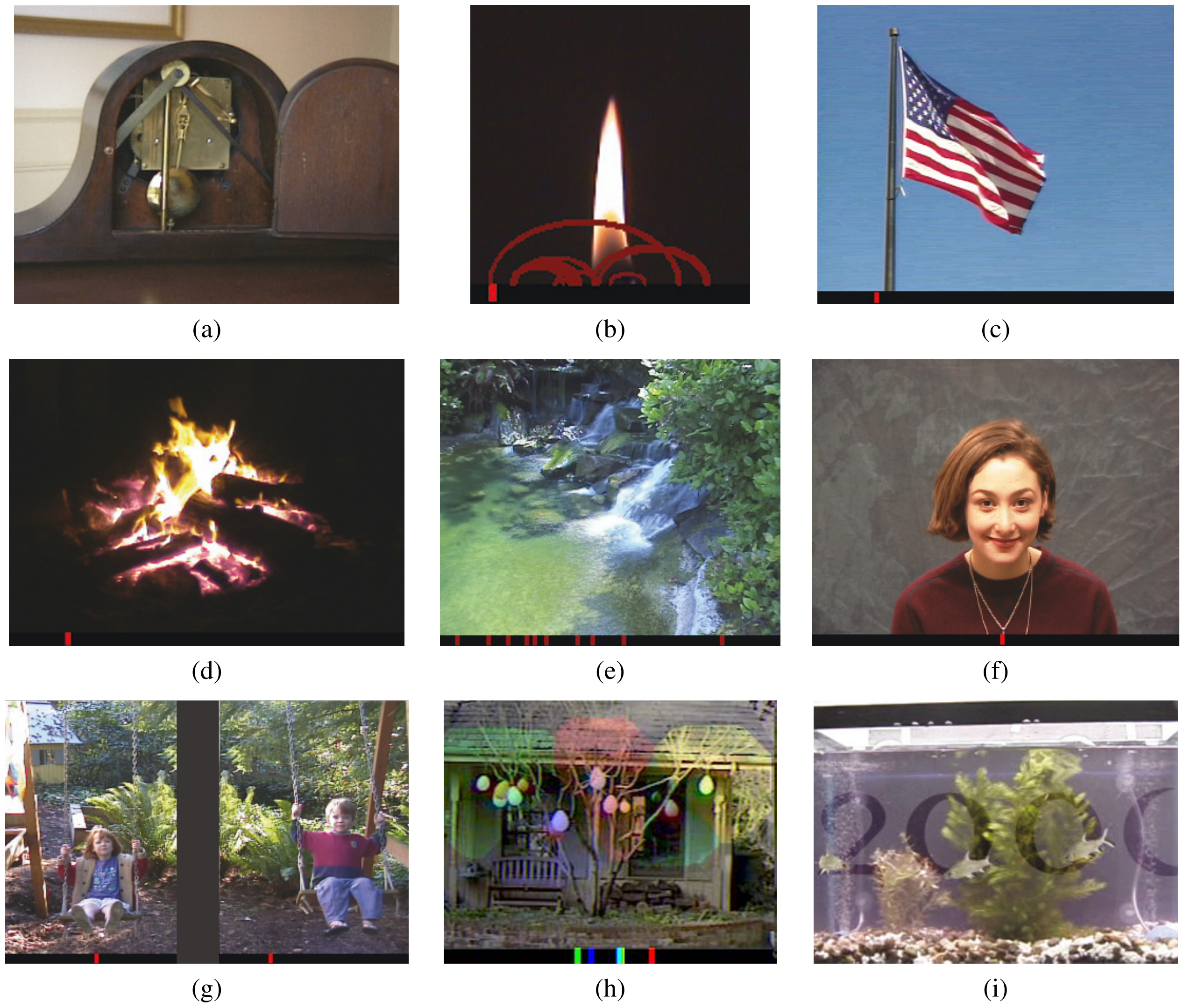

Figure 14.17 Video textures (Schödl, Szeliski *et al.* 2000) © 2000 ACM: (a) a clock pendulum, with correctly matched direction of motion; (b) a candle flame, showing temporal transition arcs; (c) the flag is generated using morphing at jumps; (d) a bonfire uses longer cross-dissolves; (e) a waterfall cross-dissolves several sequences at once; (f) a smiling animated face; (g) two swinging children are animated separately; (h) the balloons are automatically segmented into separate moving regions; (i) a synthetic fish tank consisting of bubbles, plants, and fish. Videos corresponding to these images can be found at https://www.cc.gatech.edu/gvu/perception/projects/videotexture.

Sometimes, it is not possible to find exactly matching subsequences in the original video. In this case, morphing, i.e., warping and blending frames during transitions (Section 3.6.3) can be used to hide the visual differences (Figure 14.17c). If the motion is chaotic enough, as in a bonfire or a waterfall (Figures 14.17d–e), simple blending (extended cross-dissolves) may be sufficient. Improved transitions can also be obtained by performing 3D graph cuts on the spatio-temporal volume around a transition (Kwatra, Schödl *et al.* 2003).

Video textures need not be restricted to chaotic random phenomena such as fire, wind, and water. Pleasing video textures can be created of people, e.g., a smiling face (as in Figure 14.17f) or someone running on a treadmill (Schödl, Szeliski *et al.* 2000). When multiple people or objects are moving independently, as in Figures 14.17g–h, we must first segment the video into independently moving regions and animate each region separately. It is also possible to create large panoramic video textures from a slowly panning camera (Agarwala, Zheng *et al.* 2005; He, Liao *et al.* 2017).

Instead of just playing back the original frames in a stochastic (random) manner, video textures can also be used to create scripted or interactive animations. If we extract individual elements, such as fish in a fishtank (Figure 14.17i) into separate *video sprites*, we can animate them along prespecified paths (by matching the path direction with the original sprite motion) to make our video elements move in a desired fashion (Schödl and Essa 2002). A more recent example of controlling video sprites is the Vid2Player system, which models the movements and shots of tennis players to create synthetic video-realistic games (Zhang, Sciutto *et al.* 2021). In fact, work on video textures inspired research on systems that re-synthesize new motion sequences from motion capture data, which some people refer to as "mocap soup" (Arikan and Forsyth 2002; Kovar, Gleicher, and Pighin 2002; Lee, Chai *et al.* 2002; Li, Wang, and Shum 2002; Pullen and Bregler 2002).

While video textures primarily analyze the video as a sequence of frames (or regions) that can be re-arranged in time, *temporal textures* (Szummer and Picard 1996; Bar-Joseph, El-Yaniv *et al.* 2001) and *dynamic textures* (Doretto, Chiuso *et al.* 2003; Yuan, Wen *et al.* 2004; Doretto and Soatto 2006) treat the video as a 3D spatio-temporal volume with textural properties, which can be described using auto-regressive temporal models and combined with layered representations (Chan and Vasconcelos 2009). In more recent work, video texture authoring systems have been extended to allow for control over the *dynamism* (amount of motion) in different regions (Joshi, Mehta *et al.* 2012; Liao, Joshi, and Hoppe 2013; Yan, Liu, and Furukawa 2017; He, Liao *et al.* 2017; Oh, Joo *et al.* 2017) and improved loop transitions (Liao, Finch, and Hoppe 2015).

14.5.3 *Application*: Animating pictures

While video textures can turn a short video clip into an infinitely long video, can the same thing be done with a single still image? The answer is yes, if you are willing to first segment the image into different layers and then animate each layer separately.

Chuang, Goldman *et al.* (2005) describe how an image can be decomposed into separate layers using interactive matting techniques. Each layer is then animated using a class-specific synthetic motion. As shown in Figure 14.18, boats rock back and forth, trees sway in the wind, clouds move horizontally, and water ripples, using a shaped noise displacement map. All of these effects can be tied to some global control parameters, such as the velocity and direction of a virtual wind. After being individually animated, the layers can be composited to create a final dynamic rendering.

In more recent work, Holynski, Curless *et al.* (2021) train a deep network to take a static photo, hallucinate a plausible motion field, encode the image as deep multi-resolution features, and then advect these features bi-directionally in time using Eulerian motion, using an architecture inspired by Niklaus and Liu (2020) and Wiles, Gkioxari *et al.* (2020). The resulting deep features are then decoded to produce a looping video clip with synthetic stochastic fluid motions.

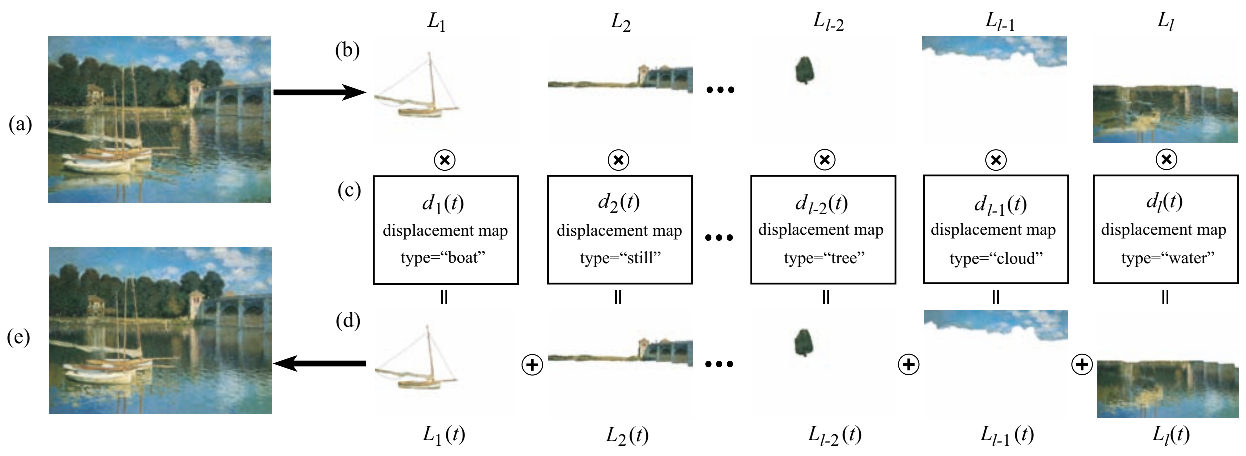
(a)
(b)
(c)
(d)
(e)
L_1
L_2
L_{l-2}
L_{l-1}
L_l
$d_1(t)$ displacement map type="boat"
$d_2(t)$ displacement map type="still"
$d_{l-2}(t)$ displacement map type="tree"
$d_{l-1}(t)$ displacement map type="cloud"
$d_l(t)$ displacement map type="water"
$L_1(t)$
$L_2(t)$
$L_{l-2}(t)$
$L_{l-1}(t)$
$L_l(t)$

Figure 14.18 Animating still pictures (Chuang, Goldman *et al.* 2005) © 2005 ACM. (a) The input still image is manually segmented into (b) several layers. (c) Each layer is then animated with a different stochastic motion texture (d) The animated layers are then composited to produce (e) the final animation

14.5.4 3D and free-viewpoint Video

In the last decade, the 3D movies have become an established medium. Currently, such releases are filmed using stereoscopic camera rigs and displayed in theaters (or at home) to viewers wearing polarized glasses. In the future, however, home audiences may wish to view such movies with multi-zone auto-stereoscopic displays, where each person gets his or her own customized stereo stream and can move around a scene to see it from different perspectives.

The stereo matching techniques developed in the computer vision community along with image-based rendering (view interpolation) techniques from graphics are both essential components in such scenarios, which are sometimes called *free-viewpoint video* (Carranza, Theobalt *et al.* 2003) or *virtual viewpoint video* (Zitnick, Kang *et al.* 2004). In addition to solving a series of per-frame reconstruction and view interpolation problems, the depth maps or proxies produced by the analysis phase must be temporally consistent in order to avoid flickering artifacts. Neural rendering techniques (Tewari, Fried *et al.* 2020, Section 6.3) can also be used for both the reconstruction and rendering phases.

Shum, Chan, and Kang (2007) and Magnor (2005) present nice overviews of various video view interpolation techniques and systems. These include the Virtualized Reality system of Kanade, Rander, and Narayanan (1997) and Vedula, Baker, and Kanade (2005), Immersive Video (Moezzi, Katkere *et al.* 1996), Image-Based Visual Hulls (Matusik, Buehler *et al.* 2000; Matusik, Buehler, and McMillan 2001), and Free-Viewpoint Video (Carranza, Theobalt *et al.* 2003), which all use global 3D geometric models (surface-based (Section 13.3) or volumetric (Section 13.5)) as their proxies for rendering. The work of Vedula, Baker, and Kanade (2005) also computes *scene flow*, i.e., the 3D motion between corresponding surface elements, which can then be used to perform spatio-temporal interpolation of the multi-view video stream. A more recent variant of scene flow is the *occupancy flow* work of Niemeyer, Mescheder *et al.* (2019).

The Virtual Viewpoint Video system of Zitnick, Kang *et al.* (2004), on the other hand, associates a two-layer depth map with each input image, which allows them to accurately model occlusion effects such as the mixed pixels that occur at object boundaries. Their system, which consists of eight synchronized video cameras connected to a disk array (Figure 14.19a), first uses segmentation-based stereo to extract a depth map for each input image (Figure 14.19e). Near object boundaries

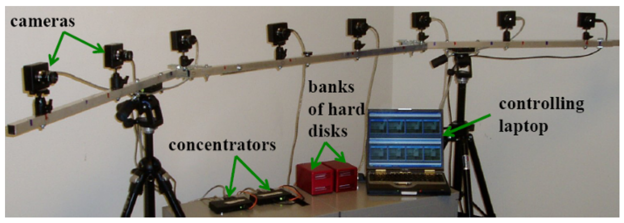

(a)

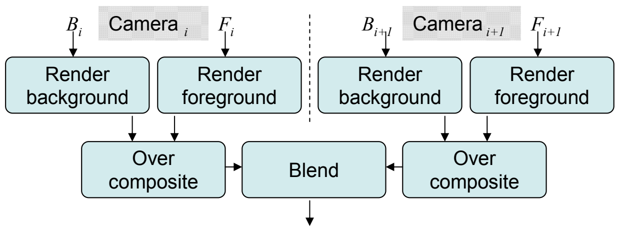

(b)

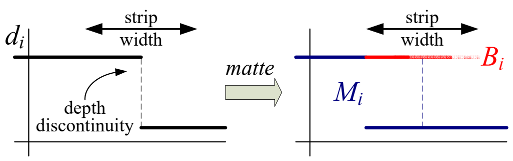

(c)

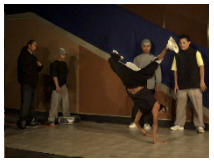

(d)

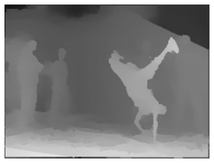

(e)

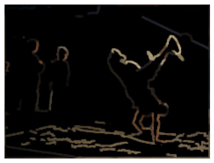

(f)

Figure 14.19 Video view interpolation (Zitnick, Kang *et al.* 2004) © 2004 ACM: (a) the capture hardware consists of eight synchronized cameras; (b) the background and foreground images from each camera are rendered and composited before blending; (c) the two-layer representation, before and after boundary matting; (d) background color estimates; (e) background depth estimates; (f) foreground color estimates.

(depth discontinuities), the background layer is extended along a strip behind the foreground object (Figure 14.19c) and its color is estimated from the neighboring images where it is not occluded (Figure 14.19d). Automated matting techniques (Section 10.4) are then used to estimate the fractional opacity and color of boundary pixels in the foreground layer (Figure 14.19f).

At render time, given a new virtual camera that lies between two of the original cameras, the layers in the neighboring cameras are rendered as texture-mapped triangles and the foreground layer (which may have fractional opacities) is then composited over the background layer (Figure 14.19b). The resulting two images are merged and blended by comparing their respective z-buffer values. (Whenever the two z-values are sufficiently close, a linear blend of the two colors is computed.) The interactive rendering system runs in real time using regular graphics hardware. It can therefore be used to change the observer's viewpoint while playing the video or to freeze the scene and explore it in 3D. Rogmans, Lu *et al.* (2009) subsequently developed GPU implementations of both real-time stereo matching and real-time rendering algorithms, which enable them to explore algorithmic alternatives in a real-time setting.

The depth maps computed from the eight stereo cameras using off-line stereo matching have been used in studies of 3D video compression (Smolic and Kauff 2005; Gotchev and Rosenhahn 2009; Tech, Chen *et al.* 2015). Active video-rate depth sensing cameras, such as the 3DV Zcam (Iddan and Yahav 2001), which we discussed in Section 13.2.1, are another potential source of such data.

When large numbers of closely spaced cameras are available, as in the Stanford Light Field Camera (Wilburn, Joshi *et al.* 2005), it may not always be necessary to compute explicit depth maps to create video-based rendering effects, although the results are usually of higher quality if you do (Vaish, Szeliski *et al.* 2006).

The last few years have seen a revival of research into 3D video, spurred in part by the wider availability of virtual reality headsets, which can be used to view such videos with a strong sense of immersion. The Jump virtual reality capture system from Google (Anderson, Gallup *et al.* 2016) uses 16 GoPro cameras arranged on a 28cm diameter ring to capture multiple videos, which are then stitched offline into a pair of omnidirectional stereo (ODS) videos (Ishiguro, Yamamoto, and Tsuji

1992; Peleg, Ben-Ezra, and Pritch 2001; Richardt, Pritch *et al.* 2013), which can then be warped at viewing time to produce separate images for each eye. A similar system, constructed from tightly synchronized industrial vision cameras, was introduced around the same time by Cabral (2016).

As noted by Anderson, Gallup *et al.* (2016), however, the ODS representation has severe limitations in interactive viewing, e.g., it does not support head tilt, or translational motion, or produce correct depth when looking up or down. More recent systems developed by Serrano, Kim *et al.* (2019), Parra Pozo, Toksvig *et al.* (2019), and Broxton, Flynn *et al.* (2020) support full 6DoF (six degrees of freedom) video, which allows viewers to move within a bounded volume while producing perspectively correct images for each eye. However, they require multi-view stereo matching during the offline construction phase to produce the 3D proxies need to support such viewing.

While these systems are designed to capture *inside out* experiences, where a user can watch a video unfolding all around them, pointing the cameras *outside in* can be used to capture one or more actors performing an activity (Kanade, Rander, and Narayanan 1997; Joo, Liu *et al.* 2015; Tang, Dou *et al.* 2018). Such setups are often called *free-viewpoint video* or *volumetric performance capture* systems. The most recent versions of such systems use deep networks to reconstruct, represent, compress, and/or render time-evolving volumetric scenes (Martin-Brualla, Pandey *et al.* 2018; Pandey, Tkach *et al.* 2019; Lombardi, Simon *et al.* 2019; Tang, Singh *et al.* 2020; Peng, Zhang *et al.* 2021), as summarized in the recent survey on neural rendering by Tewari, Fried *et al.* (2020, Section 6.3). And while most of these systems require custom-built multi-camera rigs, it is also possible to construct 3D videos from collections of handheld videos (Bansal, Vo *et al.* 2020) or even a single moving smartphone camera (Yoon, Kim *et al.* 2020; Luo, Huang *et al.* 2020).

14.5.5 *Application*: Video-based walkthroughs

Video camera arrays enable the simultaneous capture of 3D dynamic scenes from multiple viewpoints, which can then enable the viewer to explore the scene from viewpoints near the original capture locations. What if, instead we wish to capture an extended area, such as a home, a movie set, or even an entire city?

In this case, it makes more sense to move the camera through the environment and play back the video as an interactive video-based walkthrough. To allow the viewer to look around in all directions, it is preferable to use a panoramic video camera (Uyttendaele, Criminisi *et al.* 2004).[13]

One way to structure the acquisition process is to capture these images in a 2D horizontal plane, e.g., over a grid superimposed inside a room. The resulting *sea of images* (Aliaga, Funkhouser *et al.* 2003) can be used to enable continuous motion between the captured locations.[14] However, extending this idea to larger settings, e.g., beyond a single room, can become tedious and data-intensive.

Instead, a natural way to explore a space is often to just walk through it along some prespecified paths, just as museums or home tours guide users along a particular path, say down the middle of each room.[15] Similarly, city-level exploration can be achieved by driving down the middle of each street and allowing the user to branch at each intersection. This idea dates back to the Aspen MovieMap project (Lippman 1980), which recorded analog video taken from moving cars onto videodiscs for later interactive playback.

[13]See https://www.cis.upenn.edu/~kostas/omni.html for descriptions of panoramic (omnidirectional) vision systems and associated workshops.

[14]The Photo Tourism system of Snavely, Seitz, and Szeliski (2006) applies this idea to less structured collections.

[15]In computer games, restricting a player to forward and backward motion along predetermined paths is called *rail-based gaming*.

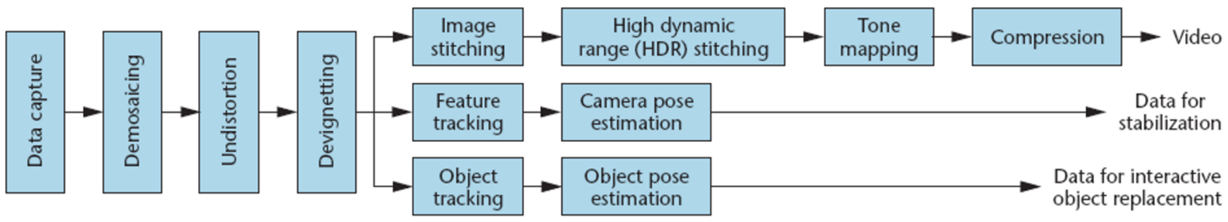

(a)

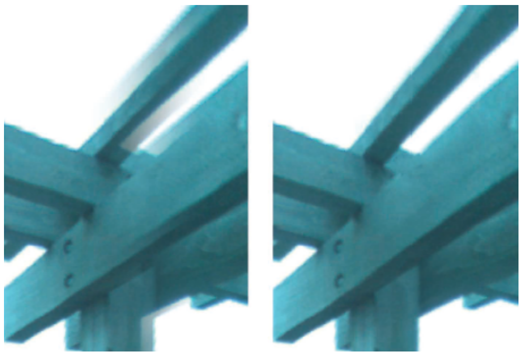
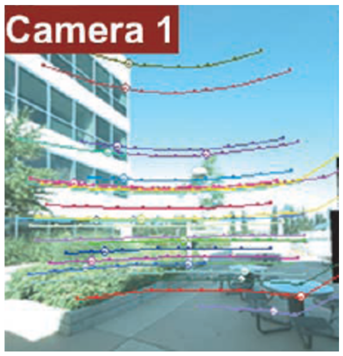

(b) (c) (d)

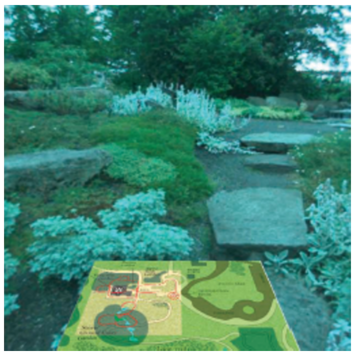
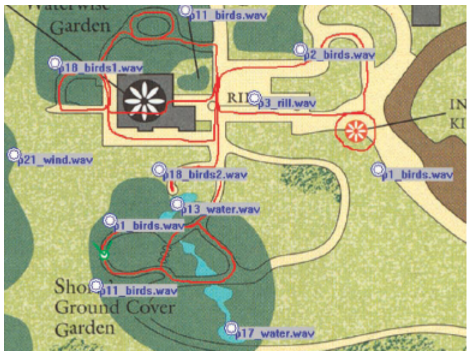

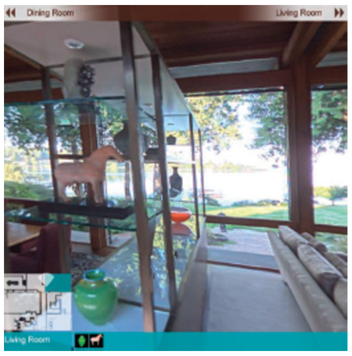

(e) (f) (g)

Figure 14.20 Video-based walkthroughs (Uyttendaele, Criminisi *et al.* 2004) © 2004 IEEE: (a) system diagram of video pre-processing; (b) the Point Grey Ladybug camera; (c) ghost removal using multi-perspective plane sweep; (d) point tracking, used both for calibration and stabilization; (e) interactive garden walkthrough with map below; (f) overhead map authoring and sound placement; (g) interactive home walkthrough with navigation bar (top) and icons of interest (bottom).

Improvements in video technology enabled the capture of panoramic (spherical) video using a small co-located array of cameras, such as the Point Grey Ladybug camera (Figure 14.20b) developed by Uyttendaele, Criminisi *et al.* (2004) for their interactive video-based walkthrough project. In their system, the synchronized video streams from the six cameras (Figure 14.20a) are stitched together into 360° panoramas using a variety of techniques developed specifically for this project.

Because the cameras do not share the same center of projection, parallax between the cameras can lead to ghosting in the overlapping fields of view (Figure 14.20c). To remove this, a multi-perspective plane sweep stereo algorithm is used to estimate per-pixel depths at each column in the overlap area. To calibrate the cameras relative to each other, the camera is spun in place and a constrained structure from motion algorithm (Figure 11.15) is used to estimate the relative camera poses and intrinsics. Feature tracking is then run on the walk-through video to stabilize the video sequence. Liu, Gleicher *et al.* (2009), Kopf, Cohen, and Szeliski (2014), and Kopf (2016) have carried out more recent work along these lines.

Indoor environments with windows, as well as sunny outdoor environments with strong shadows, often have a dynamic range that exceeds the capabilities of video sensors. For this reason, the Ladybug camera has a programmable exposure capability that enables the bracketing of exposures at subsequent video frames. To merge the resulting video frames into high dynamic range (HDR) video, pixels from adjacent frames need to be motion-compensated before being merged (Kang, Uyttendaele *et al.* 2003).

The interactive walk-through experience becomes much richer and more navigable if an overview map is available as part of the experience. In Figure 14.20f, the map has annotations, which can show up during the tour, and localized sound sources, which play (with different volumes) when the viewer is nearby. The process of aligning the video sequence with the map can be automated using a process called *map correlation* (Levin and Szeliski 2004).

All of these elements combine to provide the user with a rich, interactive, and immersive experience. Figure 14.20e shows a walk through the Bellevue Botanical Gardens, with an overview map in perspective below the live video window. Arrows on the ground are used to indicate potential directions of travel. The viewer simply orients their view towards one of the arrows (the experience can be driven using a game controller) and "walks" forward along the desired path.

Figure 14.20g shows an indoor home tour experience. In addition to a schematic map in the lower left corner and adjacent room names along the top navigation bar, icons appear along the bottom whenever items of interest, such as a homeowner's art pieces, are visible in the main window. These icons can then be clicked to provide more information and 3D views.

The development of interactive video tours spurred a renewed interest in 360° video-based virtual travel and mapping experiences, as evidenced by commercial sites such as Google's Street View and 360cities. The same videos can also be used to generate turn-by-turn driving directions, taking advantage of both expanded fields of view and image-based rendering to enhance the experience (Chen, Neubert *et al.* 2009).

While initially, 360° cameras were exotic and expensive, they have more recently become widely available consumer products, such as the popular RICOH THETA camera, first introduced in 2013, and the GoPro MAX action camera. When shooting 360° videos, it is possible to stabilize the video using algorithms tailored to such videos (Kopf 2016) or proprietary algorithms based on the camera's IMU readings. And while most of these cameras produce monocular photos and videos, VR180 cameras have two lenses and so can create wide field-of-view stereoscopic content. It is even possible to produce 3D 360° content by carefully stitching and transforming two 360° camera streams (Matzen, Cohen *et al.* 2017).

In addition to capturing immersive photos and videos of scenic locations and popular events,

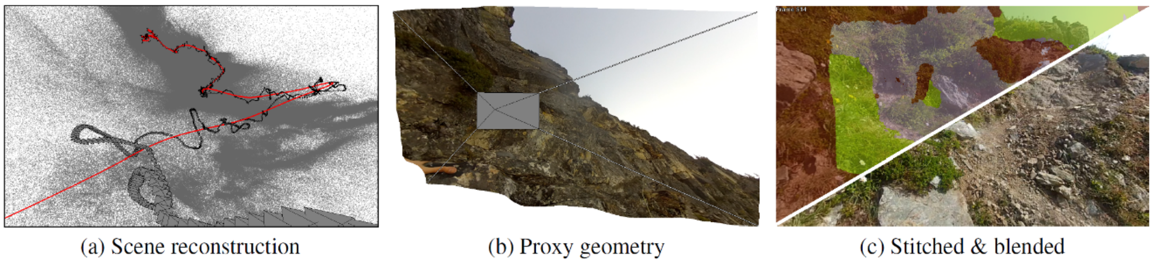

Figure 14.21 First-person hyperlapse video creation (Kopf, Cohen, and Szeliski 2014) © 2014 ACM: (a) 3D camera path and point cloud recovery, followed by smooth path planning; (b) 3D per-camera proxy estimation; and (c) source frame and seam selection using an MRF and Poisson blending.

360° and regular action cameras can also be worn, moved through an environment, and then sped up to create *hyperlapse* videos (Kopf, Cohen, and Szeliski 2014). Because such videos may exhibit large amounts of translational motion and parallax when heavily sped up, it is insufficient to simply compensate for camera rotations or even to warp individual input frames, because the large amounts of compensating motion may force the virtual camera to look outside the video frames. Instead, after constructing a sparse 3D model and smoothing the camera path, keyframes are selected and 3D proxies are computed for each of these by interpolating the sparse 3D point cloud, as shown in Figure 14.21. These frames are then warped and stitched together (using Poisson blending) using a Markov random field to ensure as much smoothness and visual continuity as possible. This system combines many different previously developed 3D modeling, computational photography, and image-based rendering algorithms to produce remarkably smooth high-speed tours of large-scale environments (such as cities) and activities (such as rock climbing and skiing).

As we continue to capture more and more of our real world with large amounts of high-quality imagery and video, the interactive modeling, exploration, and rendering techniques described in this chapter will play an even bigger role in bringing virtual experiences based in remote areas of the world as well as re-living special memories closer to everyone.

14.6 Neural rendering

The most recent development in image-based rendering is the introduction of deep neural networks into both the modeling (construction) and viewing parts of image-based rendering pipelines. Neural rendering has been applied in a number of different domains, including style and texture manipulation and 2D semantic photo synthesis (Sections 5.5.4 and 10.5.3), 3D object shape and appearance modeling (Section 13.5.1), facial animation and reenactment (Section 13.6.3), 3D body capture and replay (Section 13.6.4), novel view synthesis (Section 14.1), free-viewpoint video (Section 14.5.4), and relighting (Duchêne, Riant *et al.* 2015; Meka, Haene *et al.* 2019; Philip, Gharbi *et al.* 2019; Sun, Barron *et al.* 2019; Zhou, Hadap *et al.* 2019; Zhang, Barron *et al.* 2020).

A comprehensive survey of all of these applications and techniques can be found in the state of the art report by Tewari, Fried *et al.* (2020), whose abstract states:

> *Neural rendering is a new and rapidly emerging field that combines generative machine learning techniques with physical knowledge from computer graphics, e.g., by the integration of differentiable rendering into network training. With a plethora of applications in computer graphics and vision, neural rendering is poised to become a new area in the graphics community...*

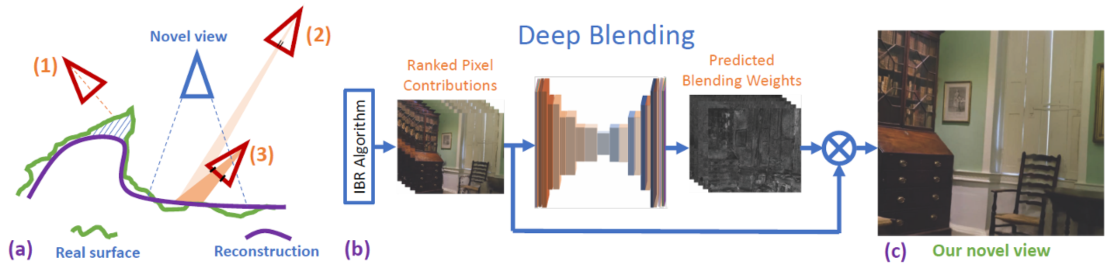

(a)

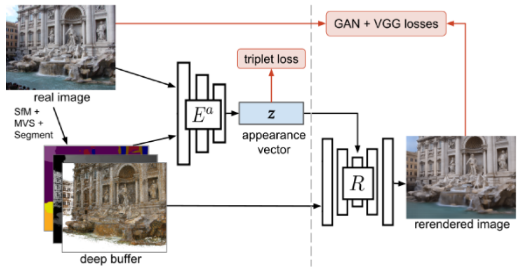

(b)

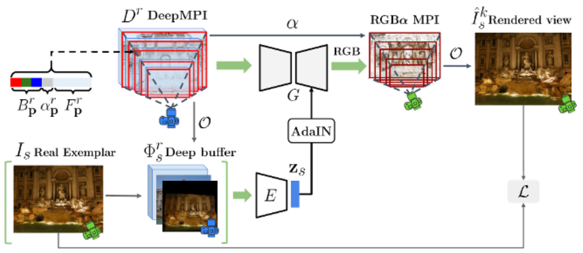

(c)

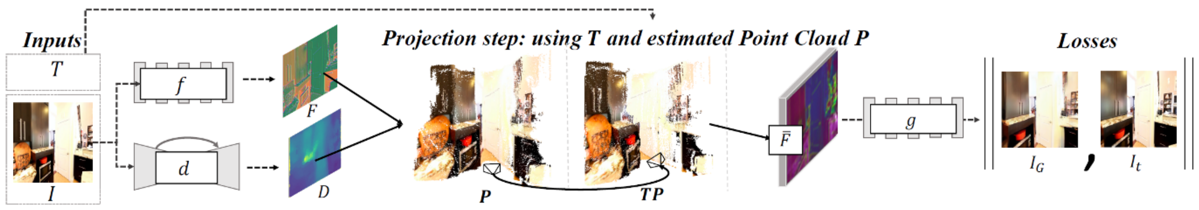

(d)

Figure 14.22 Examples of neural image-based rendering: (a) deep blending of depth-warped source images (Hedman, Philip *et al.* 2018) © 2018 ACM; (b) neural re-rendering in the wild with controllable view and lighting (Meshry, Goldman *et al.* 2019) © 2019 IEEE; (c) crowdsampling the plenoptic function with a deep MPI (Li, Xian *et al.* 2020) © 2020 Springer. (d) SynSin: novel view synthesis from a single image (Wiles, Gkioxari *et al.* 2020) © 2020 IEEE.

The survey contains over 230 references and highlights 46 representative papers, grouped into six general categories, namely semantic photo synthesis, novel view synthesis, free viewpoint video, relighting, facial reenactment, and body reenactment. As you can tell, these categories overlap with the sections of the book mentioned in the previous paragraph. A set of lectures based on this content can be found in the related CVPR tutorial on neural rendering (Tewari, Zollhöfer *et al.* 2020), and several of the lectures in the TUM AI Guest Lecture Series are also on neural rendering research.[16] The X-Fields paper by Bemana, Myszkowski *et al.* (2020, Table 1) also has a nice tabulation of related space, time, and illumination interpolation papers with an emphasis on deep methods, while the short bibliography by Dellaert and Yen-Chen (2021) summarizes even more recent techniques. Some neural rendering systems are implemented using differentiable rendering, which is surveyed by Kato, Beker *et al.* (2020).

As we have already seen many of these neural rendering techniques in the previous sections mentioned above, we focus here on their application to 3D image-based modeling and rendering. There are many ways to organize the last few years' worth of research in neural rendering. In this

[16] https://niessner.github.io/TUM-AI-Lecture-Series

section, I have chosen to use four broad categories of underlying 3D representations, which we have studied in the last two chapters, namely: texture-mapped meshes, depth images and layers, volumetric grids, and implicit functions.

Texture-mapped meshes. As described in Chapter 13, a convenient representation for modeling and rendering a 3D scene is a triangle mesh, which can be reconstructed from images using multi-view stereo. One of the earliest papers to use a neural network as part of the 3D rendering process was the deep blending system of Hedman, Philip *et al.* (2018), who augment an unstructured Lumigraph rendering pipeline (Buehler, Bosse *et al.* 2001) with a deep neural network that computes the per-pixel blending weights for the warped images selected for each novel view, as shown in Figure 14.22a. LookinGood (Martin-Brualla, Pandey *et al.* 2018) takes a single or multiple-image texture-mapped 3D upper or whole-body rendering and fills in the holes, denoises the appearance, and increases the resolution using a U-Net trained on held out views. Along a similar line, Deep Learning Super Sampling (DLSS) uses an encoder-decoder DNN implemented in GPU hardware to increase the resolution of rendered games in real time (Burnes 2020).

While these systems warp colored textures or images (i.e., view-dependent textures) and then apply a neural net post-process, it is also possible to first convert the images into a "neural" encoding and then warp and blend such representations. Free View Synthesis (Riegler and Koltun 2020a) starts by building a local 3D model for the novel view using multi-view stereo. It then encodes the source images as neural codes, reprojects these codes to the novel viewpoint, and composites them using a recurrent neural network and softmax. Instead of warping neural codes at render time and then blending and decoding them, the follow-on Stable View Synthesis system (Riegler and Koltun 2020b) collects neural codes from all incoming rays for every surface point and then combines these with an *on-surface aggregation* network to produce outgoing neural codes along the rays to the novel view camera. Deferred Neural Rendering (Thies, Zollhöfer, and Nießner 2019) uses a (u, v) parameterization over the 3D surface to learn and store a 2D texture map of neural codes, which can be sampled and decoded at rendering time.

Depth images and layers. To deal with images taken at different times of day and weather, i.e., "in the wild", Meshry, Goldman *et al.* (2019) use a DNN to compute a latent "appearance" vector for each input image and its associated depth image (computed using traditional multi-view stereo), as shown in Figure 14.22b. At render time, the appearance can be manipulated (in addition to the 3D viewpoint) to explore the range of conditions under which the images were taken. Li, Xian *et al.* (2020) develop a related pipeline (Figure 14.22c), which instead of storing a single "deep" color/depth/appearance image or buffer uses a multiplane image (MPI). As with the previous system, an encoder-decoder modulated with the appearance vector (using Adaptive Instance Normalization) is used to render the final image, in this case through an intermediate MPI that does the view warping and over compositing. Instead of using many parallel finely sliced planes, the GeLaTO (Generative Latent Textured Objects) system uses a small number of oriented planes ("billboards") with associated neural textures to model thin transparent objects such as eyeglasses (Martin-Brualla, Pandey *et al.* 2020). At render time, these textures are warped and then decoded and composited using a U-Net to produce a final RGBA sprite.

While all of these previous systems use multiple images to build a 3D neural representation, SynSin (Synthesis from a Single Image) (Wiles, Gkioxari *et al.* 2020) starts with just a single color image and uses a DNN to turn this image into a neural features F and depth D buffer pair, as shown in Figure 14.22d. At render time, the neural features are warped according to their associated depths and the camera view matrix, splatted with soft weights, and composited back-to-front to obtain a

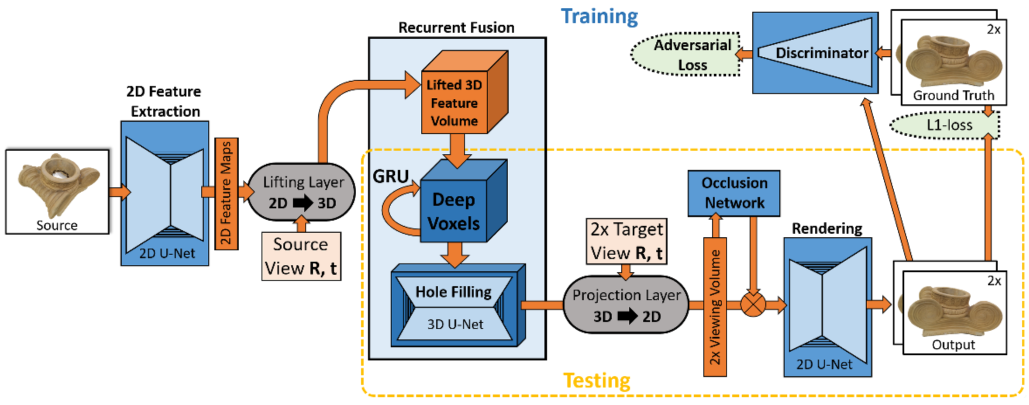

(a)

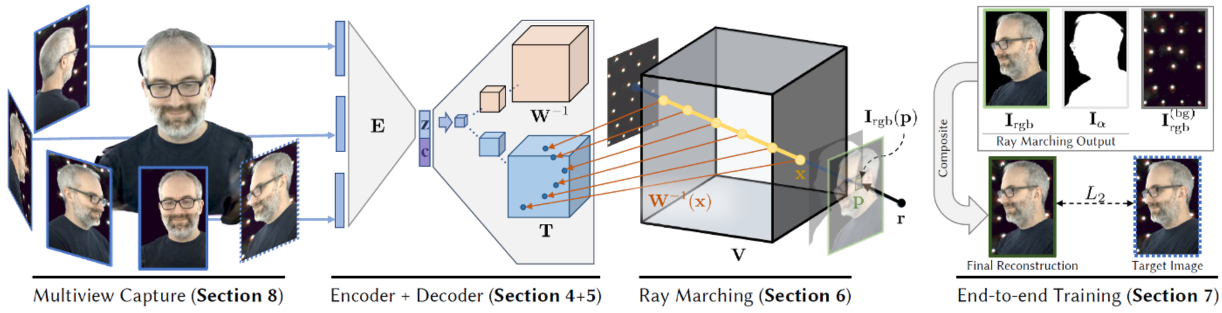
E
z
c
$\mathbf{W}^{-1}$
T
$\mathbf{I}_{\text{rgb}}(\mathbf{p})$
$\mathbf{W}^{-1}(\mathbf{x})$
x
p
r
V
$\mathbf{I}_{\text{rgb}}$
$\mathbf{I}_{\alpha}$
$\mathbf{I}^{(\text{bg})}_{\text{rgb}}$
Ray Marching Output
Composite
L_2
Final Reconstruction
Target Image
Multiview Capture (Section 8)
Encoder + Decoder (Section 4+5)
Ray Marching (Section 6)
End-to-end Training (Section 7)

(b)

Figure 14.23 Examples of voxel grid neural rendering: (a) DeepVoxels (Sitzmann, Thies *et al.* 2019) © 2019 IEEE; (b) Neural Volumes (Lombardi, Simon *et al.* 2019) © 2019 ACM.

neural rendered frame $\tilde{F}$, which is then decoded into the final color novel view I_G. In Semantic View Synthesis Huang, Tseng *et al.* (2020) start with a semantic label map and use semantic image synthesis (Section 5.5.4) to convert this into a synthetic color image and depth map. These are then used to create a multiplane image from which novel views can be rendered. Holynski, Curless *et al.* (2021) train a deep network to take a static photo, hallucinate a plausible motion field, encode the image as deep features with soft blending weights, advect these features bi-directionally in time, and decode the rendered neural feature frames to produce a looping video clip with synthetic stochastic fluid motions, as discussed in Section 14.5.3.

Voxel representations. Another 3D representation that can be used for neural rendering is a 3D voxel grid. Figure 14.23 shows the modeling and rendering pipelines from two such papers. DeepVoxels (Sitzmann, Thies *et al.* 2019) learn a 3D embedding of neural codes for a given 3D object. At render time, these are projected into 2D view, filtered through an occlusion network (similar to back-to-front alpha compositing), and then decoded into a final image. Neural Volumes (Lombardi, Simon *et al.* 2019) use an encoder-decoder to convert a set of multi-view color images into a 3D RGBα volume and an associated volumetric warp field that can model facial expression variation. At render time, the color volume is warped and then ray marching is used to create a final 2D RGBα foreground image.[17] In more recent work, Weng, Curless, and Kemelmacher-Shlizerman

[17]Note that we mostly use RGBA in earlier parts of the book to denote three color channels with an opacity. In the remainder of this section, I use RGBα to be consistent with recent papers.

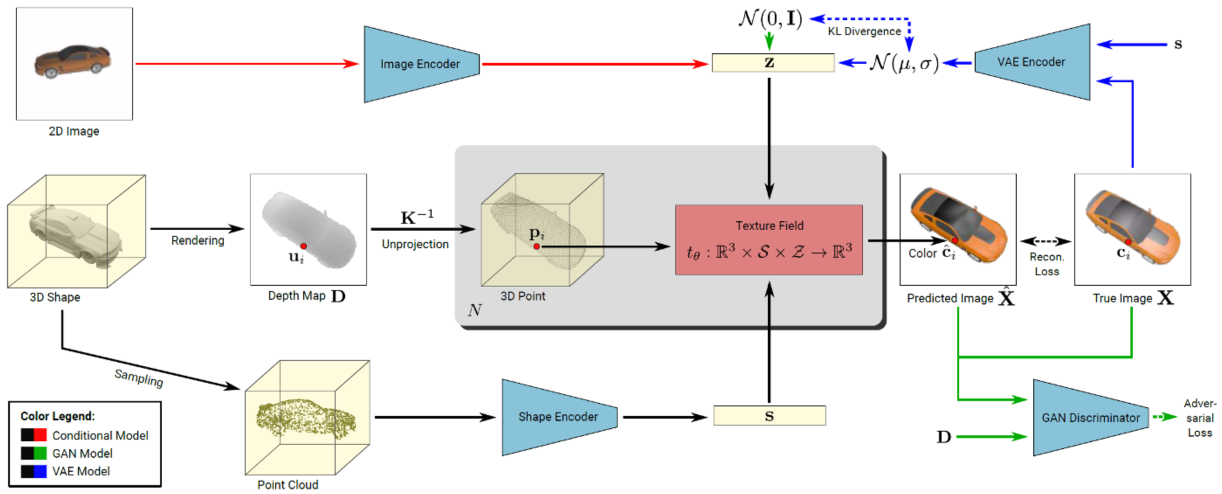

(a)

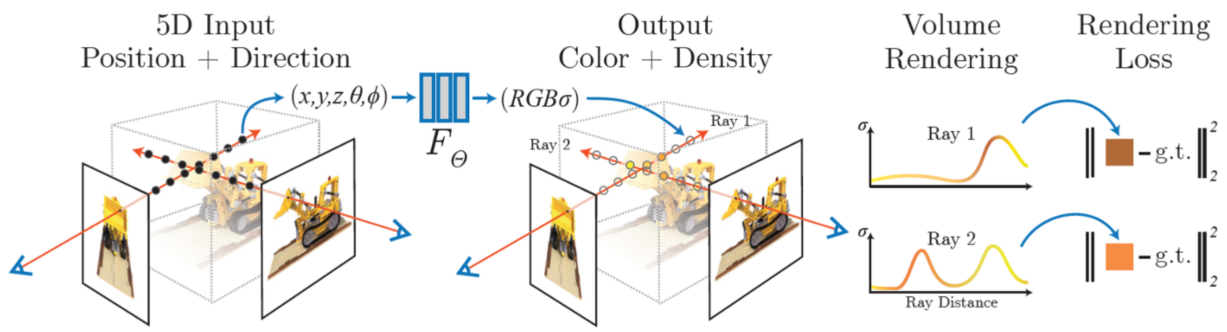

(b)

Figure 14.24 Examples of implicit function (MLP) neural rendering: (a) Texture Fields (Oechsle, Mescheder *et al.* 2019) © 2019 IEEE; (b) Neural Radiance Fields (Mildenhall, Srinivasan *et al.* 2020) © 2020 Springer.

(2020) show how deformable Neural Volumes can be constructed and animated from monocular videos of moving people, such as athletes.

Coordinate-based neural representations. The final representation we discuss in this section are implicit functions implemented using fully connected networks, which are now more commonly known as *multilayer perceptrons* or MLPs.[18] We have already seen the use of $[0,1]$ occupancy and implicit signed distance functions for 3D shape modeling in Section 13.5.1, where we mentioned papers such as Occupancy Networks (Mescheder, Oechsle *et al.* 2019), IM-NET (Chen and Zhang 2019), DeepSDF (Park, Florence *et al.* 2019), and Convolutional Occupancy Networks (Peng, Niemeyer *et al.* 2020).

To render colored images, such representations also need to encode the appearance (e.g., color, texture, or light field) information at either the surface or throughout the volume. Texture Fields (Oechsle, Mescheder *et al.* 2019) train an MLP conditioned on both 3D shape and latent appearance (e.g., car color) to produce a 3D volumetric color field that can then be used to texture-map a 3D

[18] As Jon Barron and others have pointed out, only signed distance functions actually encode “implicit functions” as level-sets of their volumetric values. The more general class of techniques that includes opacity models is often called *coordinate regression networks* or *coordinate-based MLPs*.

model, as shown in Figure 14.24a. This representation can be extended using differentiable rendering to directly compute depth gradients, as in Differential Volumetric Rendering (DVR) (Niemeyer, Mescheder *et al.* 2020). Pixel-aligned Implicit function (PIFu) networks (Saito, Huang *et al.* 2019; Saito, Simon *et al.* 2020) also use MLPs to compute volumetric inside/outside and color fields and can hallucinate full 3D models from just a single color image, as shown in Figure 13.18. Scene representation networks (Sitzmann, Zollhöfer, and Wetzstein 2019) use an MLP to map volumetric (x, y, z) coordinates to high-dimensional neural features, which are used by both a ray marching LSTM (conditioned on the 3D view and output pixel coordinate) and a 1×1 color pixel decoder to generate the final image. The network can interpolate both appearance and shape latent variables.

An interesting hybrid system that replaces a trained per-object MLP with on-the-fly multi-view stereo matching and image-based rendering is the IBRNet system of Wang, Wang *et al.* (2021). As with other volumetric neural renders, the network evaluates each ray in the novel viewpoint image by marching along the ray and computing a density and neural appearance feature at each sampled location. However, instead of looking up these values from a pre-trained MLP, it samples the neural features from a small number of adjacent input images, much like in Unstructured Lumigraph (Buehler, Bosse *et al.* 2001; Hedman, Philip *et al.* 2018) and Stable View Synthesis (Riegler and Koltun 2020b), which use a precomputed 3D surface model (which IBRNet does not). The opacity and appearance values along the ray are refined using a transformer architecture, which replaces the more traditional winner-take-all module in a stereo matcher, followed by a classic volumetric compositing of the colors and densities.

To model viewpoint dependent effects such as highlights on plastic objects, i.e., to model a full light field (Section 14.3), Neural Radiance Fields (NeRF) extend the implicit mapping from (x, y, z) spatial positions to also include a viewing direction (θ, ϕ) as inputs, as shown in Figure 14.24b (Mildenhall, Srinivasan *et al.* 2020). Each (x, y, z) query is first turned into a *positional encoding* that consists of sinusoidal waves at octave frequencies before going into a 256-channel MLP. These positional codes are also injected into the fifth layer, and an encoding of the viewing direction is injected at the ninth layer, which is where the opacities are computed (Mildenhall, Srinivasan *et al.* 2020, Figure 7). It turns out that these positional encodings are essential to enabling the MLP to represent fine details, as explored in more depth by Tancik, Srinivasan *et al.* (2020), as well as in the SIREN (Sinusoidal Representation Network) paper by Sitzmann, Martel *et al.* (2020), which uses periodic (sinusoidal) activation functions.

It is also possible to pre-train these neural networks, i.e., use *meta-learning*, on a wider class of objects to speed up the optimization task for new images (Sitzmann, Chan *et al.* 2020; Tancik, Mildenhall *et al.* 2021) and also to use cone tracing together with *integrated positional encoding* to reduce aliasing and handle multi-resolution inputs and output (Barron, Mildenhall *et al.* 2021). The NeRF++ paper by Zhang, Riegler *et al.* (2020) extends the original NeRF representation to handle unbounded 3D scenes by adding an "inside-out" $1/r$ *inverted sphere parameterization*, while Neural Sparse Voxel Fields build an octree with implicit neural functions inside each non-empty cell (Liu, Gu *et al.* 2020).

Instead of modeling opacities, the Implicit Differentiable Renderer (IDR) developed by Yariv, Kasten *et al.* (2020) models a signed distance function, which enables them at rendering time to extract a level-set surface with analytic normals, which are then passed to the neural renderer, which models viewpoint-dependent effects. The system also automatically adjusts input camera positions using differentiable rendering. Neural Lumigraph Rendering uses sinusoidal representation networks to produce more compact representations (Kellnhofer, Jebe *et al.* 2021). They can also export a 3D mesh for much faster view-dependent Lumigraph rendering. Takikawa, Litalien *et al.* (2021) also construct an implicit signed distance field, but instead of using a single MLP, they build a sparse octree structure that stores neural features in cells (much like neural sparse voxel fields) and supports both level of detail and fast sphere tracing. Neural Implicit Surfaces (NeuS) also use a signed distance representation but use a rendering formula that better handles surface occlusions (Wang, Liu *et al.* 2021).

While NeRF, IDR, and NSVF require a large number of images of a static object taken under controlled (uniform lighting) conditions, NeRF in the Wild (Martin-Brualla, Radwan *et al.* 2021) takes an unstructured set of images from a landmark tourist location and not only models appearance changes such as weather and time of day but also removes transient occluders such as tourists. NeRFs can also be constructed from a single or small number of images by conditioning a class-specific neural radiance field on such inputs as in pixelNeRF (Yu, Ye *et al.* 2020). Deformable neural radiance fields or "nerfies" (Park, Sinha *et al.* 2020), Neural Scene Flow Fields (Li, Niklaus *et al.* 2021), Dynamic Neural Radiance Fields (Pumarola, Corona *et al.* 2021), Space-time Neural Irradiance Fields (Xian, Huang *et al.* 2021), and HyperNeRF (Park, Sinha *et al.* 2021) all take as input hand-held videos taken around a person or moving through a scene. They model both the viewpoint variation and volumetric non-rigid deformations such as head or body movements and expression changes, either using a learned deformation field, adding time as an extra input variable, or embedding the representation in a higher dimension.

It is also possible to extend NeRFs to model not only the opacities and view-dependent colors of 3D coordinates, but also their interactions with potential illuminants. Neural Reflectance and Visibility Fields (NeRV) do this by also returning for each query 3D coordinate a surface normal and parametric BRDF as well as the environment visibility and expected termination depth for outgoing rays at that point (Srinivasan, Deng *et al.* 2021). Neural Reflection Decomposition (NeRD) models densities and colors using an implicit MLP that also returns an appearance vector, which is decoded into a parametric BRDF (Boss, Braun *et al.* 2020). It then uses the environmental illumination, approximated using spherical Gaussians, along with the density normal and BRDF, to render the final color sample at that voxel. PhySG uses a similar approach, using a signed distance field to represent the shape and a mixture of spherical Gaussian to represent the BRDF (Zhang, Luan *et al.* 2021).

Most of the neural rendering techniques that include view-dependent effects are quite slow to render, since they require sampling a volumetric space along each ray, using expensive MLPs to perform each location/direction lookup. To achieve real-time rendering while modeling view-dependent effects, a number of recent papers use efficient spatial data structures (octrees, sparse grids, or multiplane images) to store opacities and base colors (or potentially small MLPs) and then use factored approximations of the radiance field to model view-dependent effects (Wizadwongsa, Phongthawee *et al.* 2021; Garbin, Kowalski *et al.* 2021; Reiser, Peng *et al.* 2021; Yu, Li *et al.* 2021; Hedman, Srinivasan *et al.* 2021). While the exact details of the representations used in the various stages vary amongst these papers, they all start with high-fidelity view-dependent models related to the original NeRF paper or its extensions and then "bake" or "distill" these into faster to evaluate spatial data structures and simplified (but still accurate) view-dependent models. The resulting systems produce the same high fidelity renderings as full Neural Radiance Fields while running often 1000x faster than pure MLP-based representations.

As you can tell from the brief discussion in this section, neural rendering is an extremely active research area with new architectures being proposed every few months (Dellaert and Yen-Chen 2021). The best place to find the latest developments, as with other topics in computer vision, is to look on arXiv and in the leading computer vision, graphics, and machine learning conferences.

14.7 Additional reading

Two good surveys of image-based rendering are by Kang, Li *et al.* (2006) and Shum, Chan, and Kang (2007), with earlier surveys available from Kang (1999), McMillan and Gortler (1999), and Debevec (1999). Today, the field often goes under the name of *novel view synthesis* (NVS), with a recent tutorial at CVPR (Gallo, Troccoli *et al.* 2020) providing a good overview of historical and current techniques.

The term *image-based rendering* was introduced by McMillan and Bishop (1995), although the seminal paper in the field is the view interpolation paper by Chen and Williams (1993). Debevec, Taylor, and Malik (1996) describe their Façade system, which not only created a variety of image-based modeling tools but also introduced the widely used technique of *view-dependent texture mapping*. Early work on planar impostors and layers was carried out by Shade, Lischinski *et al.* (1996), Lengyel and Snyder (1997), and Torborg and Kajiya (1996), while newer work based on *sprites with depth* is described by Shade, Gortler *et al.* (1998). Using a large number of parallel planes with RGBA colors and opacities (originally dubbed the "stack of acetates" model by Szeliski and Golland (1999)) was rediscovered by Zhou, Tucker *et al.* (2018) and now goes by the name of multiplane images (MPI). This representation is widely used in recent 3D capture and rendering pipelines (Mildenhall, Srinivasan *et al.* 2019; Choi, Gallo *et al.* 2019; Broxton, Flynn *et al.* 2020; Attal, Ling *et al.* 2020; Lin, Xu *et al.* 2020). To accurately model reflections, the alpha-compositing operator used in MPIs needs to be replaced with an additive model, as in Sinha, Kopf *et al.* (2012) and Kopf, Langguth *et al.* (2013).

The two foundational papers in image-based rendering are *Light field rendering* by Levoy and Hanrahan (1996) and *The Lumigraph* by Gortler, Grzeszczuk *et al.* (1996). Buehler, Bosse *et al.* (2001) generalize the Lumigraph approach to irregularly spaced collections of images, while Levoy (2006) provides a survey and more gentle introduction to the topic of light field and image-based rendering. Wu, Masia *et al.* (2017) provide a more recent survey of this topic. More recently, neural rendering techniques have been used to improve the blending heuristics used in the Unstructured Lumigraph (Hedman, Philip *et al.* 2018; Riegler and Koltun 2020a).

Surface light fields (Wood, Azuma *et al.* 2000; Park, Newcombe, and Seitz 2018; Yariv, Kasten *et al.* 2020) provide an alternative parameterization for light fields with accurately known surface geometry and support both better compression and the possibility of editing surface properties. Concentric mosaics (Shum and He 1999; Shum, Wang *et al.* 2002) and panoramas with depth (Peleg, Ben-Ezra, and Pritch 2001; Li, Shum *et al.* 2004; Zheng, Kang *et al.* 2007), provide useful parameterizations for light fields captured with panning cameras. Multi-perspective images (Rademacher and Bishop 1998) and manifold projections (Peleg and Herman 1997), although not true light fields, are also closely related to these ideas.

Among the possible extensions of light fields to higher-dimensional structures, environment mattes (Zongker, Werner *et al.* 1999; Chuang, Zongker *et al.* 2000) are the most useful, especially for placing captured objects into new scenes.

Video-based rendering, i.e., the re-use of video to create new animations or virtual experiences, started with the seminal work of Szummer and Picard (1996), Bregler, Covell, and Slaney (1997), and Schödl, Szeliski *et al.* (2000). Important follow-on work to these basic re-targeting approaches includes Schödl and Essa (2002), Kwatra, Schödl *et al.* (2003), Doretto, Chiuso *et al.* (2003), Wang and Zhu (2003), Zhong and Sclaroff (2003), Yuan, Wen *et al.* (2004), Doretto and Soatto (2006), Zhao and Pietikäinen (2007), Chan and Vasconcelos (2009), Joshi, Mehta *et al.* (2012), Liao, Joshi, and Hoppe (2013), Liao, Finch, and Hoppe (2015), Yan, Liu, and Furukawa (2017), He, Liao *et al.* (2017), and Oh, Joo *et al.* (2017). Related techniques have also been used for performance driven video animation (Zollhöfer, Thies *et al.* 2018; Fried, Tewari *et al.* 2019; Chan, Ginosar *et al.* 2019;

Egger, Smith *et al.* 2020).

Systems that allow users to change their 3D viewpoint based on multiple synchronized video streams include Moezzi, Katkere *et al.* (1996), Kanade, Rander, and Narayanan (1997), Matusik, Buehler *et al.* (2000), Matusik, Buehler, and McMillan (2001), Carranza, Theobalt *et al.* (2003), Zitnick, Kang *et al.* (2004), Magnor (2005), Vedula, Baker, and Kanade (2005), Joo, Liu *et al.* (2015), Anderson, Gallup *et al.* (2016), Tang, Dou *et al.* (2018), Serrano, Kim *et al.* (2019), Parra Pozo, Toksvig *et al.* (2019), Bansal, Vo *et al.* (2020), Broxton, Flynn *et al.* (2020), and Tewari, Fried *et al.* (2020). 3D (multi-view) video coding and compression is also an active area of research (Smolic and Kauff 2005; Gotchev and Rosenhahn 2009), and is used in 3D Blu-Ray discs and multi-view video coding (MVC) extensions to the High Efficientcy Video Coding (HEVC) standard (Tech, Chen *et al.* 2015).

The whole field of neural rendering is quite recent, with initial publications focusing on 2D image synthesis (Zhu, Krähenbühl *et al.* 2016; Isola, Zhu *et al.* 2017) and only more recently being applied to 3D novel view synthesis (Hedman, Philip *et al.* 2018; Martin-Brualla, Pandey *et al.* 2018). Tewari, Fried *et al.* (2020) provide an excellent survey of this area, with 230 references and 46 highlighted papers. Additional overviews include the related CVPR tutorial on neural rendering (Tewari, Zollhöfer *et al.* 2020), several of the lectures in the TUM AI Guest Lecture Series, the X-Fields paper by Bemana, Myszkowski *et al.* (2020, Table 1), and a recent bibliography by Dellaert and Yen-Chen (2021).

14.8 Exercises

Ex 14.1: Depth image rendering. Develop a "view extrapolation" algorithm to re-render a previously computed stereo depth map coupled with its corresponding reference color image.

1. Use a 3D graphics mesh rendering system such as OpenGL with two triangles per pixel quad and perspective (projective) texture mapping (Debevec, Yu, and Borshukov 1998).

2. Alternatively, use the one- or two-pass forward warper you constructed in Exercise 3.24, extended using (2.68–2.70) to convert from disparities or depths into displacements.

3. (Optional) Kinks in straight lines introduced during view interpolation or extrapolation are visually noticeable, which is one reason why image morphing systems let you specify line correspondences (Beier and Neely 1992). Modify your depth estimation algorithm to match and estimate the geometry of straight lines and incorporate it into your image-based rendering algorithm.

Ex 14.2: View interpolation. Extend the system you created in the previous exercise to render two reference views and then blend the images using a combination of z-buffering, hole filing, and blending (morphing) to create the final image (Section 14.1).

1. (Optional) If the two source images have very different exposures, the hole-filled regions and the blended regions will have different exposures. Can you extend your algorithm to mitigate this?

2. (Optional) Extend your algorithm to perform three-way (trilinear) interpolation between neighboring views. You can triangulate the reference camera poses and use barycentric coordinates for the virtual camera to determine the blending weights.

Ex 14.3: View morphing. Modify your view interpolation algorithm to perform morphs between views of a non-rigid object, such as a person changing expressions.

1. Instead of using a pure stereo algorithm, use a general flow algorithm to compute displacements, but separate them into a rigid displacement due to camera motion and a non-rigid deformation.

2. At render time, use the rigid geometry to determine the new pixel location but then add a fraction of the non-rigid displacement as well.

3. (Optional) Take a single image, such as the Mona Lisa or a friend's picture, and create an animated 3D view morph (Seitz and Dyer 1996).

   (a) Find the vertical axis of symmetry in the image and reflect your reference image to provide a virtual pair (assuming the person's hairstyle is somewhat symmetric).
   (b) Use structure from motion to determine the relative camera pose of the pair.
   (c) Use dense stereo matching to estimate the 3D shape.
   (d) Use view morphing to create a 3D animation.

Ex 14.4: View dependent texture mapping. Use a 3D model you created along with the original images to implement a view-dependent texture mapping system.

1. Use one of the 3D reconstruction techniques you developed in Exercises 11.10, 12.9, 12.10, or 13.8 to build a triangulated 3D image-based model from multiple photographs.

2. Extract textures for each model face from your photographs, either by performing the appropriate resampling or by figuring out how to use the texture mapping software to directly access the source images.

3. For each new camera view, select the best source image for each visible model face.

4. Extend this to blend between the top two or three textures. This is trickier, because it involves the use of texture blending or pixel shading (Debevec, Taylor, and Malik 1996; Debevec, Yu, and Borshukov 1998; Pighin, Hecker *et al.* 1998).

Ex 14.5: Layered depth images. Extend your view interpolation algorithm (Exercise 14.2) to store more than one depth or color value per pixel (Shade, Gortler *et al.* 1998), i.e., a layered depth image (LDI). Modify your rendering algorithm accordingly. For your data, you can use synthetic ray tracing, a layered reconstructed model, or a volumetric reconstruction.

Ex 14.6: Rendering from sprites or layers. Extend your view interpolation algorithm to handle multiple planes or sprites (Section 14.2.1) (Shade, Gortler *et al.* 1998).

1. Extract your layers using the technique you developed in Exercise 9.7.

2. Alternatively, use an interactive painting and 3D placement system to extract your layers (Kang 1998; Oh, Chen *et al.* 2001; Shum, Sun *et al.* 2004).

3. Determine a back-to-front order based on expected visibility or add a z-buffer to your rendering algorithm to handle occlusions.

4. Render and composite all of the resulting layers, with optional alpha matting to handle the edges of layers and sprites.

5. Try one of the newer multiplane image (MPI) techniques (Zhou, Tucker *et al.* 2018).

Ex 14.7: Light field transformations. Derive the equations relating regular images to 4D light field coordinates.

1. Determine the mapping between the far plane (u, v) coordinates and a virtual camera's (x, y) coordinates.
   (a) Start by parameterizing a 3D point on the uv plane in terms of its (u, v) coordinates.
   (b) Project the resulting 3D point to the camera pixels $(x, y, 1)$ using the usual 3×4 camera matrix $\mathbf{P}$ (2.63).
   (c) Derive the 2D homography relating (u, v) and (x, y) coordinates.
2. Write down a similar transformation for (s, t) to (x, y) coordinates.
3. Prove that if the virtual camera is actually on the (s, t) plane, the (s, t) value depends only on the camera's image center and is independent of (x, y).
4. Prove that an image taken by a regular orthographic or perspective camera, i.e., one that has a linear projective relationship between 3D points and (x, y) pixels (2.63), samples the (s, t, u, v) light field along a two-dimensional hyperplane.

Ex 14.8: Light field and Lumigraph rendering. Implement a light field or Lumigraph rendering system:

1. Download one of the light field datasets from http://lightfield.stanford.edu or https://lightfield-analysis.uni-konstanz.de.
2. Write an algorithm to synthesize a new view from this light field, using quadri-linear interpolation of (s, t, u, v) ray samples.
3. Try varying the focal plane corresponding to your desired view (Isaksen, McMillan, and Gortler 2000) and see if the resulting image looks sharper.
4. Determine a 3D proxy for the objects in your scene. You can do this by running multi-view stereo over one of your light fields to obtain a depth map per image.
5. Implement the Lumigraph rendering algorithm, which modifies the sampling of rays according to the 3D location of each surface element.
6. Collect a set of images yourself and determine their pose using structure from motion.
7. Implement the unstructured Lumigraph rendering algorithm from Buehler, Bosse *et al.* (2001).

Ex 14.9: Surface light fields. Construct a surface light field (Wood, Azuma *et al.* 2000) and see how well you can compress it.

1. Acquire an interesting light field of a specular scene or object, or download one from http://lightfield.stanford.edu or https://lightfield-analysis.uni-konstanz.de.
2. Build a 3D model of the object using a multi-view stereo algorithm that is robust to outliers due to specularities.
3. Estimate the Lumisphere for each surface point on the object.

4. Estimate its diffuse components. Is the median the best way to do this? Why not use the minimum color value? What happens if there is Lambertian shading on the diffuse component?

5. Model and compress the remaining portion of the Lumisphere using one of the techniques suggested by Wood, Azuma *et al.* (2000) or invent one of your own.

6. Study how well your compression algorithm works and what artifacts it produces.

7. (Optional) Develop a system to edit and manipulate your surface light field.

Ex 14.10: Handheld concentric mosaics. Develop a system to navigate a handheld concentric mosaic.

1. Stand in the middle of a room with a camcorder held at arm's length in front of you and spin in a circle.

2. Use a structure from motion system to determine the camera pose and sparse 3D structure for each input frame.

3. (Optional) Re-bin your image pixels into a more regular concentric mosaic structure.

4. At view time, determine from the new camera's view (which should be near the plane of your original capture) which source pixels to display. You can simplify your computations to determine a source column (and scaling) for each output column.

5. (Optional) Use your sparse 3D structure, interpolated to a dense depth map, to improve your rendering (Zheng, Kang *et al.* 2007).

Ex 14.11: Video textures. Capture some videos of natural phenomena, such as a water fountain, fire, or smiling face, and loop the video seamlessly into an infinite length video (Schödl, Szeliski *et al.* 2000).

1. Compare all the frames in the original clip using an L_2 (sum of square difference) metric. (This assumes the videos were shot on a tripod or have already been stabilized.)

2. Filter the comparison table temporally to accentuate temporal sub-sequences that match well together.

3. Convert your similarity table into a jump probability table through some exponential distribution. Be sure to modify transitions near the end so you do not get "stuck" in the last frame.

4. Starting with the first frame, use your transition table to decide whether to jump forward, backward, or continue to the next frame.

5. (Optional) Add any of the other extensions to the original video textures idea, such as multiple moving regions, interactive control, or graph cut spatio-temporal texture seaming.

Ex 14.12: Neural rendering. Most of the recent neural rendering papers come with open source code as well as carefully acquired datasets.

Try downloading more than one of these and run different algorithms on different datasets. Compare the quality of the renderings you obtain and list the visual artifacts you detect and how you might improve them.

Try capturing your own dataset, if this is feasible, and describe additional breaking points of the current algorithms.